Referee #1 (Hartwig Deneke)
Received and published: 20 July 2022

Note: The page and line numbers used in the response are referring to the revised manuscript (track-change version), which is appended to this response.

General comments

C: The article describes a Python project for 3D radiative transfer, the EaR^{3}T toolbox. While somewhat technical in scope, the article is generally well written, likely of interest to a wider scientific audience, and falls within the scope of AMT. There are however a few aspects which could be improved, which I list below. Hence, I recommend publication of the article after minor revisions.
R: Thank you very much for your comments.

Specific comments

C: For reproducibility, I strongly recommend to obtain a DOI for the described version of the code in the github repository, e.g. via Zenodo, see https://docs.github.com/en/repositories/archiving-a-github-repository/referencing-and-citing-content. While the article mentions "in the current version", no clear information on versioning of the code is given, this needs to be rectified, in particular, the article needs to clarify which version of the code is referred to.
R: Thank you very much for your suggestions and providing instructions. We have released the first official version of EaR^{3}T (version 0.1.0) on Github (https://www.github.com/hong-chen/er3t/releases/tag/v0.1.0) and obtained DOI from Zenodo (doi:10.5281/zenodo.7374196). The information has been updated in the revised manuscript (Page 9, Line 244).

C: Usage of APP for application: why not App? It's used as an abbreviation, not as an acronym.
R: We have changed the "APP" in "App." In the revised manuscript to avoid confusion between abbreviation and acronym.

C: As mentioned in the text, APP5 is not described, but it is included in Fig.1. I propose to also remove it from Fig.1. The description "four of which are described in this paper" at least for me raises the question why, maybe motivate this choice somewhat?
R: Thank you. The reason we included App. 5 in Figure 1 is that we believe context-aware CNN algorithms based on machine learning will become the key towards the mitigation of 3D cloud retrieval bias, where EaR^{3}T shines by its automation capability of creating extensive simulation datasets for training CNN. We decided to keep App. 5 in Figure 1 and added a brief description of CNN in Appendix B with the details discussed by Nataraja et al. (2022). We hope after adding in

descriptions of CNN in the Appendix B (Page 43, Line 1174), we can keep App. 5 in Figure 1 to keep the information complete from the two papers (this paper and Nataraja et al., 2022).

C: Summary and Outlook: I do find the outlook somewhat too short/lacking a clear vision about future development of the code. The following sentence also raises some questions: "EaR^{3}T will continue to be an educational tool driven by graduate students." I did not find anything indicating which parts of the code so far have been actually written by graduate students (who of the authors is at that stage?), given that several co-authors are rather senior. I also would assume that it takes someone with significant experience to maintain such a project in the long term. Please elaborate at least to some detail on these points.
R: Thank you. We added some text (Page 39, Line 1127) regarding future work of adding support for more publicly available 3D RT solvers, e.g., SHDOM and MYSTIC, and built-in support for HITRAN. The current version of EaR^{3}T including code base and applications were solely developed by graduate student Hong Chen (first author of this paper) under the advisement of Prof. Sebastian Schmidt. The other authors of this paper contributed the data and model used in the four applications of EaR^{3}T. Currently, a few other applications of EaR^{3}T, e.g., spectral simulations for OCO-2, are under development by other graduate students in Prof. Schmidt's group. To keep the continuity, Hong Chen is committed to maintain EaR^{3}T for the next few years and gradually transition the development and maintenance of EaR^{3}T to other graduate students in Prof. Schmidt's group. We added "Author contribution" in the revised manuscript (Page 48, Line 1289).

C: Please also note the following minor language comments:
L264: "MODIS is currently flying on ..." I doubt this will change anytime soon, rephrase sentence?
R: We rephrased the sentence into "The MODIS instruments are multi-use multispectral radiometers onboard …" (Page 13, Line 326).

C: L265: "They are ...": Please clarify "They", I guess it refers to MODIS.
R: Yes, it refers to MODIS. We changed "They are …" to "MODIS was …" for clarification (Page 13, Line 327).

References:

Nataraja, V., Schmidt, S., Chen, H., Yamaguchi, T., Kazil, J., Feingold, G., Wolf, K., and Iwabuchi, H.: Segmentation-Based Multi-Pixel Cloud Optical Thickness Retrieval Using a Convolutional Neural Network, Atmos. Meas. Tech., 15, 5181–5205, doi:10.5194/amt-15-5181-2022, 2022.

Referee #2 (Anonymous Referee)
Received and published: 31 August 2022

Note: The page and line numbers used in the response are referring to the revised manuscript (track-change version), which is appended to this response.

Text

C: The paper introduces the versatile EaR^{3}T Radiative Transfer Toolbox and showcases several applications with focus on analyzing and mitigating 3D effects in observations and simulations. I thank the authors for this overall very nice paper. I particularly find its education targeted approach very interesting. I have few, both general and specific, comments (see below) and recommend to publish the paper when these overall minor issues are addressed.
R: Thank you very much for your comments.

General comments

C: Some, as I understand, mandatory or highly recommended sections are missing, incl. Data availability and Author contributions.
R: We have added sections of data availability and author contributions into the manuscript.

C: As the other reviewer pointed out, it would be highly desirable if code & examples used here are available from a long-term archive.
R: Purposing for reproducibility and traceability, we have made a public release of EaR^{3}T (version 0.1.0) on GitHub (https://github.com/hong-chen/er3t/releases/tag/v0.1.0) and obtained DOI from Zenodo (doi: 10.5281/zenodo.7374196). The information has been updated in the revised manuscript (Page 9, Line 244).

C: You characterize EaR^{3}T as "automated" and running with "minimal user input" and stated that "automation of EaR^{3}T permits calculations at any time and over any region". Could you be a bit more specific, what you mean by that (automated)? On the one hand, please summarize, what user input is actually needed (what is mandatory, what optional) and how the user has to provide/setup. What does the user interface look like, how does it work? An example of a call/setup could be helpful, e.g. illustrating how the Tab2 settings (at least for one APP are realized). Also, how is the model executed; e.g. how are the steps mentioned in L425f executed? Does the user have to do that with a script, is there a ready-made script available, ...? Make clear, what is the "normal" way to do these things with EaR^{3}T.
R: Thank you for your comments. The regular ("normal") operation of 3D or 1D radiative transfer calculations is usually done by passing the required parameters through a parameter list contained within a formatted text or binary file along with auxiliary data in a format specific to an RT solver. This requires the user to manually adjust the input files, prepare the auxiliary data, and post process the output. The automation of EaR^{3}T minimizes these manual efforts by providing functions that

can contain the parameter input within a programming language (here Python), where unlimited operations, e.g., loops, can be achieved through programming. Additionally, with the functions (offered by EaR^{3}T) that can preprocess of the auxiliary data, e.g., surface setup, clouds setup, aerosol setup etc., and postprocess of the results can be integrated, which, combined, provides automation capability. In other words, EaR^{3}T serves as a 'wrapper' to RT code, including the pre-processing and downloading of input data, and including the post-processing – but it is also more than that because it can be run along entire aircraft flight tracks or satellite orbits. The automation does not mean EaR^{3}T takes away user's freedom of specifying parameters – parameters can be specified as detailed as possible that the RT solver supports. Instead, EaR^{3}T offers flexibility to bypassing some parameters through defaults. For example, if the cloud geometric thickness is not available or specified, EaR^{3}T will use a default value (1km), which however can be controlled by the user. This allows the user to arrive at simulations without much hassle. In a way, this is similar to the RT library of libRadtran, where certain parameters can be set as "standard", and others are implicit. The input parameters that the user can control (or their defaults) were added to the manuscript for better transparency – in Appendix A in the revised manuscript. The example codes (contains interface of the code) along with guide of how to install and run are distributed along with EaR^{3}T. The example codes distributed along with EaR^{3}T are ready-to-run once setup. The example codes are designed so they can be easily adapted for related projects (e.g., for a different wavelength). Currently, the application of EaR^{3}T for completely new project that cannot be created by adapting one of the pre-existing example codes will still require some support from the author of EaR^{3}T and of this paper. This will hopefully be improved once the documentation is more complete in the future. The execution is done at the example code level, e.g., "python 02_modis_rad-sim.py" under <examples> directory will reproduce the results in Figure 6 in the manuscript, which processes involve MODIS data downloading, preprocessing of surface and cloud setup based on MODIS products, running 3D RT, and postprocessing the outputs.

C: On the other hand, "with minimal user input" implies that many parameter that need to be known for radiative transfer model are implicitly assumed (aka "hardcoded") - which are these and what setting/assumptions are made there? What effects do these assumptions have on the RT results?

R: To address this comment as well as the following few comments, we added Appendix A (Page 40, Line 1135), which provides a detailed list of controllable parameters and their default settings for each application. The effects of these assumption on the RT results are discussed in the other comments of this response.

C: Also, certain manual adjustments/user settings are obviously still necessary, e.g. setting of an (appropriate) SZA. I lack an overview of these additional required setup beyond time & location. Also, I'd appreciate some remarks on the ease or difficulty to adapt the examples to more or less different applications e.g. the use of different sensor channels.

R: The current SZA settings for App. 1 and App. 2 are using the average of SZA of observations by default. It can indeed be set differently by user. As we mentioned in our response to the previous comment, we added a detailed list of controllable parameters and their default settings for each application in Appendix A. Current example code supports simple adjustments for a slightly different application, e.g., a different wavelength of the same sensor. However, for an independent project, a different example code needs to be developed (combining the functions of EaR^3T in different ways) [see comment above; this will currently require support from the author].

C: One exemplary aspect here: you do not seem to consider, e.g., cloud vertical location & extent as "user input", although that needs to be specified somehow and at least partly seems to require an "educated guess" by the user, which in turn introduces a user dependent source of uncertainty.
R: In fact, EaR^3T can ingest the atmospheric information as detailed as the underlying RT solver can offer. For example, if cloud vertical location is available from active or passive remote sensing, EaR^3T can put the clouds at the correct location. If it is not known and not provided by the user, then this information is superseded by default values as explained above. However, for transparency reasons, we included a new appendix (see comment above).

C: The example scene contains different cloud types (from low to vertically extended). Here I would like to see a short discussion on the effect of fixed cloud geo thickness in the setup. How realistic is the 1km-thick-clouds setting in APP1&2 (also considering that the clouds in this scene all seem to be high-level clouds according to Fig3c (CTH>8km)? How sensitive are the outputs to this, ie what errors can result from that? How realistic is that for the cumulonimbus contained in the scene? Similarly, for APP3&4, what uncertainties do the cloud location choices induce; how sensitive are results to those choices (considering they might be off by a few km for individual clouds in a scene and that those seemingly need to be chosen by the user beforehand. what about (frequently occurring) multi-level clouds?
R: The 1km-thick-clouds assumption would only be valid for the low-level thin clouds and would not be realistic for cumulonimbus (CTH>8km). To evaluate the sensitivity to this assumption, we performed another 3D RT run with cloud base at 0.5km for all the clouds (clouds vertically extend from 0.5km to cloud top height). The radiance difference between the new run and the run with 1km-thick-clouds assumption is shown in the following Figure (Figure 6-extra-1). The figure indicates that when the clouds have a larger vertical extent, more horizontal photon transport, leading to an even larger 3D effect that for shallow clouds, i.e., smaller radiances in the core of the nimbus. Since we were looking at nadir radiance/reflectance, the radiance difference for tall vs. shallow clouds is smaller than from oblique viewing angles where the vertical structure of the clouds matters even more. We added the following discussion short discussion in the revised manuscript (Page 26, Line 734)
"It should be pointed out that the vertical extent of the clouds affects the simulated radiance – the larger the vertical extent, the larger the 3D effects (more horizontal photon transport). Since we make the assumption of a cloud geometric thickness of 1 km if no thickness information is provided, the simulated radiance at the satellite sensor level is valid for that proxy cloud only. For deeper clouds, the simulated radiance would be even lower. Either way, the comparison with the actual radiance measurements will reveal a lack of closure."
For App. 3, the uncertainties associated with 1km-thick-clouds is small because we are looking at the downwelling irradiance below clouds. For App. 4, the 1km-thick-clouds should work as the cloud location of 1km to 2km is estimated from the aircraft observations. For the applications we provided in the manuscript, the assumptions are relatively safe (nadir radiance/reflectance, transmittance, selected camera imagery). This does not mean that, when using EaR^3T, one has to live with assumptions. Our goal is not to fill in missing data, but use data wherever it is available,

and subsequently use the radiance consistency approach to determine how accurate and appropriate these data and any assumptions were. EaR^{3}T offers the capability to digest the details of the atmosphere if they are available, but it can also run if they are not – through the aforementioned assumptions. For global application (e.g., multi-layer clouds, aerosols, surfaces), a dedicated effort needs to be invested into developing a much more comprehensive example code than the one we discussed in the manuscript, but this is all doable using the functions provided by EaR^{3}T. We are envisioning that with more data resources (e.g., observations from active remote sensing, 3D atmospheric retrievals (Barker et al., 2011)) and EaR^{3}T and methodologies provided in the manuscript, we can arrive at 3D radiation closure at a global scale.

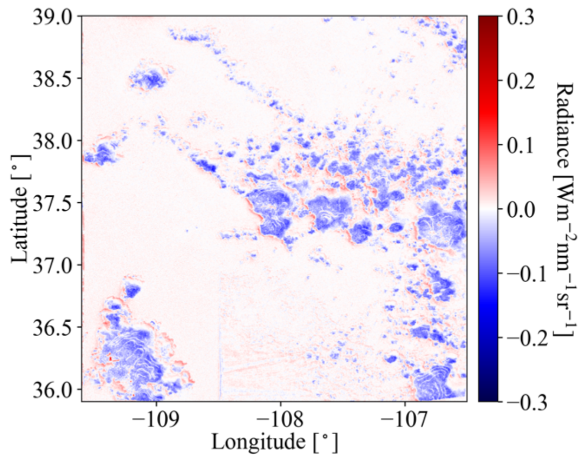

Figure 6-extra-1: Radiance difference between simulations using clouds 1) extending from 0.5 km to cloud top height (Radiance1) and 2) assuming clouds are 1km thick (Radiance2). The difference is Radiance1 minus Radiance2.

C: In Sec.3, I have some difficulties to understand, how exactly cloud extinction, phase, and Reff calculated from the input data? From which input data, specifically?

R: The cloud extinction, phase function, and cloud effective radius are processed during the pre-processing step. EaR^{3}T contains functions to process these cloud properties on application basis. For example, for satellite applications, EaR^{3}T offers functions to download the satellite data and extract cloud properties from satellite products, or directly use cloud retrievals obtained from tailored algorithms developed by user (e.g., two-stream approximation for obtaining high resolution cloud optical thickness field from radiance observations). For LES applications, EaR^{3}T offers functions that can extract the cloud optical properties from LES data itself.

C: What input parameters are required for MCARaTS, specifically? How are they derived from the pre-processed cloud & surface properties – is this just a re-gridding, or does it require a(nother) parameter transformation? How would that (need to be) different for libRadtran? Some equations would be helpful here.

R: The MCARaTS requires the inputs of radiative properties of surface and atmospheric constituents (e.g., gases, aerosols, clouds) such as single scattering albedo, scattering phase function, or asymmetry parameters, along with solar and sensor viewing geometries. We added descriptions of input parameters for MCARaTS in the revised manuscript (Page 9, Line 245). Those optical properties are not directly contained within satellite products. The preprocessing is a parameter transformation that converts indirect atmospheric properties (e.g., cloud optical thickness and cloud effective radius) into direct optical properties of the atmospheric constituents (e.g., absorption coefficients, extinction coefficients, single scattering albedo, scattering phase function, asymmetry parameters etc.) that MCARaTS can digest. Meanwhile, the preprocessing also makes formatted input text file and auxiliary data files that contain RT parameters required by MCARaTS. For libRadtran, a different wrapper is developed within EaR^{3}T to cope with input parameters required by libRadtran in a different format than MCARaTS.

C: What determines the RT grid – in the horizontal as well as in the vertical? User input? Input data resolution?
R: On the input side, the vertical grid of the RT is set by the user during the atmospheric profile setup step in the pre-processing. For the vertical grid, corresponding atmospheric profile of gas concentration will be extracted (if not specified, the AFGL US standard atmosphere will be used – see Appendix A), then gas absorption coefficient profile will be extracted. Later, the clouds, aerosols will be inserted into the vertical grid through linear interpolation while the extinction coefficients will go through sum/average to ensure the column-integrated property is consistent before and after re-gridding. From the output side, the irradiance/flux will output at vertical grid set by user while the radiance will output with horizontal grid defined by the horizontal grid of cloud field.

C: Sort out, explain, and correctly use your terminology: Specifically, for App4 (and summary item c), disentangle IPA/2-stream vs. 3D/CNN (why does Fig11 talk about COT estimated by IPA, Fig12 of COT estimated by 2-stream? That's the same data from the same method, isn't it?).
R: The words of <3D and CNN> and <IPA and Two-Stream> were used interchangeably in APP4 (COT mentioned in Figure 11 (IPA) and Figure 12 (two-stream) are the same). We changed the wording to achieve better clarification and consistency so now in APP4, we only use <CNN> and <IPA>.

C: Avoid the impression to claim that EaR^{3}T is the only 3D-RT capable model/tool(box) (aeg around L848) – there is and has been for a long while a variety of those. libRadTran/MYSTIC, SASKTRAN (Bourassa08), McSCIA (Spada06), and SPARTA (Barlakas16) in the solar radiation part of the spectrum as well as e.g. ARTS (Buehler18) in the MW/IR region are just a few that come to mind. Also, there's the WCRP's I3RC project (Cahalan04; https://www.wcrp-climate.org/modelling-wgcm-mip-catalogue/modelling-wgcm-mips-2/261-modelling-wgcm-catalogue-i3rc). Please put your model/toolbox in context with those.
R: Thank you for providing the references. We briefly discussed related 3D radiative transfer solvers and toolboxes in the introduction of the revised manuscript (Page 4, Line 104), but not all of the ones that were proposed. For example, the Buehler code is applicable for the IR (to our knowledge), and our manuscript focuses on the SW.

Specific comments

Add axis labels incl. unit specification to all figures, and colorbars to all 2D plots.
R: We added units and/or colorbars for all the figures in the revised manuscript.

Fig1/L201f: Improve color coding explanation: I had to read a couple of time to get, e.g., the difference between black & blue coded surface albedo and what the relation between input data & pre-processing step color coding is.
R: We added legend for color coding explanation (Figure 1, Page 7, Line 182). Additionally, we changed surface albedo associated processes in blue for consistency. The color-coded data products under Data Acquisition were fed into the pre-processing associated with 1) surface setup in blue, 2) clouds setup in brown, and 3) providing ground truth in green.

L203f: Explicitly point out/summarize, what input is required by MCARaTS.
R: We added some description of MCARaTS inputs in the revised manuscript (Page 9, Line 245).

Tab1: Why is radiance limited to 2D output?
R: The radiance calculations are performed for a given altitude. Thus, the output is 2D (along x and y) *without* vertical dimension.

L238: I like your scene selection and the corresponding reasoning a lot. However, the results are not (yet?) analyzed and discussed explicitly for those diverse conditions. Maybe a few summarizing word on performance depending on the different surface & cloud types could be added?
R: We added some discussion (Page 26, Line 742 and Page 40, Line 1157) in the revised manuscript about the challenges associated with the complexity of the surface.

L290f: Clarify relation of surface reflectance and surface albedo; how is (RT-input?) albedo converted from (observed) reflectance? Does it imply an assumption on surface reflection type (Lambertian?).
R: The surface reflectance is directly used as surface albedo input to the RTM assuming a Lambertian surface. We added clarification in the manuscript (see Page 14, Line 372).

L310ff: Are 10m winds really a good proxy for cloud altitude winds? What about using AMV for the wind correction?
R: 10m wind might indeed not be the optimal choice for accurately accounting for the cloud movements. Using Atmospheric Motion Vectors (AMV) is a good idea for better representing the cloud movements in the wind correction step. Since we only aimed at providing a bare-bones structure of approaches in this paper and 10m wind speed data was readily available from the OCO-2 data archive, we performed the wind correction using the 10m wind speed only. In the

future, we will fine-tune each approach (e.g., improve cloud detection algorithm, improve parallax correction and wind correction etc.) to get into a detailed inter-comparison between observations and simulations. Actually, a few members within our group are conducting such development, e.g., cloud detection in the Arctic, and the work will be published in the near-future.

Fig3: What from are the fine white lines in the figure (eg at lon ~ -108.0 between lat ~ 37.4-37.6)? Correctional shift artifacts? Are those indeed treated as clear-sky then?

R: The white lines (cracks) are artifacts from the parallax correction. Yes, those were treated as clear-sky in the RTM. These white cracks can be avoided if we 1) turn off the parallax correction; 2) coarsen the study domain (for example, from 250m in the manuscript to 500m); or 3) improve parallax correction by taking adjacent pixels into account. In this version of EaR^{3}T, 2) or 3) have not been implemented.

L330: Why only a slope is fitted, not an offset, too? Looking at Fig4b it seems to me, a steeper slope with negative bias (passing through the two maxima) would fit the data better. Do you have any hypothesis on the origin of the two occurrence maxima? Would a surface type dependent fitting/transformation possibly be better?

R: If with offset, when surface albedo of x channel is 0 (e.g., a pure dark scene), the y channel will arrive at offset as surface albedo for the same pure dark scene, which is not physically reasonable, especially when the offset is negative. The following Figure shows the location of OCO-2 measured surface reflectance and collocated surface reflectance from MODIS surface product. The data is divided into two categories – OCO-2 surface radiance greater than 0.23 (upper maximum) in red and OCO-2 surface reflectance smaller-equal to 0.23 (lower maxima). We assume that such patterns might be associated with imperfect cloud filtering in 8-day MODIS surface reflectance product (based on our experience). The surface parameterization (linear regression) we developed is an imperfect but working solution to arrive at satellite radiance simulations. In the continuation work of OCO-2 as mentioned in the manuscript, we can improve surface reflectance parameterization by, e.g., using MODIS surface albedo product and performing surface type dependent fitting/transformation.

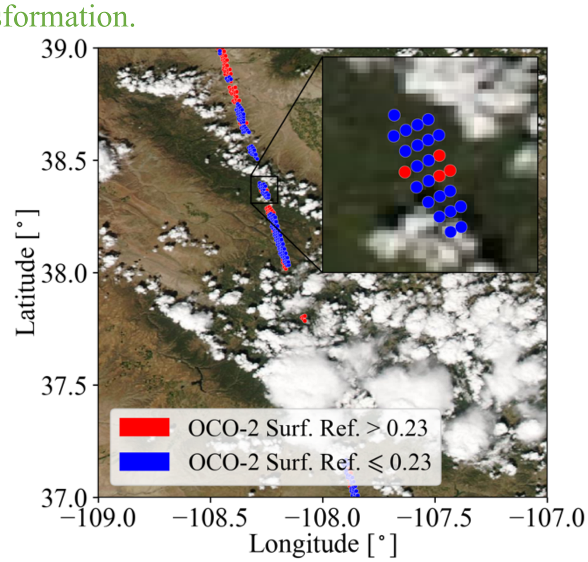

Figure 4-extra: The same as Figure 2 in the manuscript except for circles indicating the location of OCO-2 surface reflectance observations with larger values in red (> 0.23) and lower values (≤ 0.23) in blue.

L332: Are the same fitted-a values used for the other two channels, or do you just refer to the same fitting procedure?
R: The same fitting procedure can be applied for other OCO-2 channels – in this paper, only a channel of Oxygen-A band of three OCO-2 bands (Oxygen-A, stong-CO_2, weak-CO_2) is discussed. We decided to remove the text to avoid confusion.

L440: I don't get that sentence. Does "each wavelength" here refer to monochromatic wavelengths? Or individual channels? What are the "hundreds of individual absorption coefficient profiles"? why are they spectrally spaced for "each wavelength"?
R: The reviewer is correct. We changed the text as follows to clarify: "For each OCO-2 spectrometer wavelength within a given channel, hundreds of …" (Page 19, Line 541). In other words, there are three levels here: (1) OCO-2 channel (Oxygen A-Band, Weak CO2 band, Strong CO2 band), (2) spectrometer-resolution wavelengths in each band, (3) ABSCO line-resolving spectral spacing. For each of the spectrometer-resolution wavelengths (2), hundreds of wavelengths from ABSCO (3) need to be considered. After the calculations are done, all those individual calculations are convolved using the ILS.

L462: Again, what is the "target wavelength"? A channel?
R: The reviewer is correct. The "target wavelength" here means a channel. We added the text "(this could either be an individual SSFR or a MODIS channel)" (Page 20, Line 574) for clarification.

L502f: Could you shortly mention, how the parallelization can be applied (incl. install requirements & how to control the use of the parallelization) and whether the APPs in their current setup use this feature?
R: There are two kinds of parallelization that can be achieved – from RT solver side and from EaR^3T side. The RT-solver-side parallelization requires additional software libraries (e.g., OpenMPI) during the installation setup. The parallelization of EaR^3T is done through multi-processing, thus is natively supported (with EaR^3T itself). Yes, the APPs (in their current setup) does use parallelization by default. We clarified this in the newly added Appendix A in the revised manuscript (Page 40, Line 1140).

Fig5: Why is this done on latitude-averaged rather than on footprint base? As the text argues with it (for cloudy locations; L544), could you (also) provide an equivalent plot on footprint base? A difference plot could be helpful, too. Why is there no spread/uncertainty shading on the IPA results? What is the range of SZA in the observations within the plot range?
R: We did latitude-averaging because the footprints of OCO-2 are not orthogonal to the latitude/longitude. We provided the OCO-2 vs simulation (IPA) intercomparison over the specified domain at footprint base and added it as Figure 5b in the revised manuscript. Additionally, we

added the uncertainty shading for the IPA simulations. The SZA of the observations ranges from 32.59° to 34.92° with an average of 33.57°.

Fig6: Again, what is the range of SZA in the observations over the scene? What is the errors/uncertainties introduced by using a fixed SZA in the simulations?

R: The solar zenith angle (SZA) of the observations over the scene ranges from 32.43° to 36.46° with an average of 34.42°. To evaluate the errors/uncertainties, we performed the simulation at 32.43° (SZA_{Min}) and 36.46° (SZA_{Max}) in addition to 34.42° (SZA_{Mean}). Figure 6-extra-2 (the following figure) shows the reflectance (hemispherically integrated radiance normalized by cosine of SZA) of (a) SZA_{Min} vs SZA_{Mean} and (b) SZA_{Max} vs SZA_{Mean}. Linear regression (y=ax) is performed and shown in black line. For SZA_{Min} vs SZA_{Mean}, the fitted slope is 0.995. For SZA_{Max} vs SZA_{Mean}, the fitted slope is 1.002. In other words, we are getting errors on the order of <0.5% in the domain average from the variability of the SZA throughout the area. The one-sigma errors of both are minimal – 0.000045. Thus we think the errors/uncertainties introduced by SZA in the simulations are minimal.

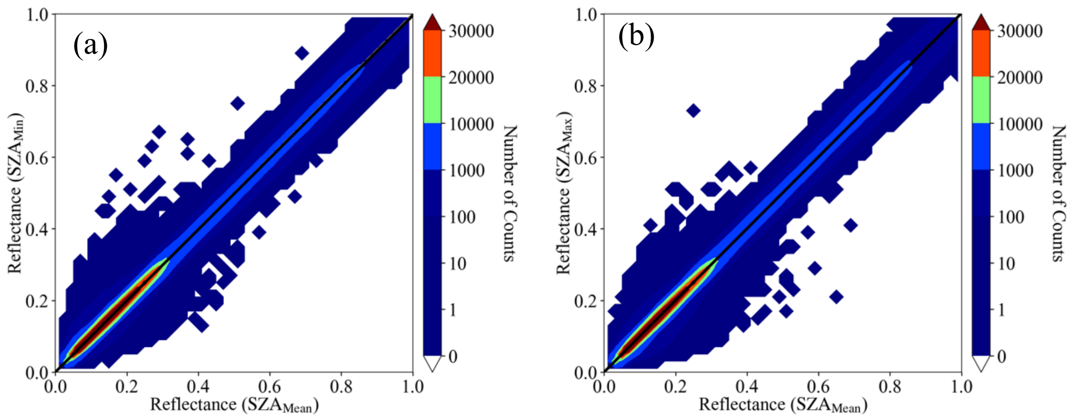

Figure 6-extra-2: **(a)** Simulated Reflectance at SZA=32.43° (SZA_{Min}) vs Simulated Reflectance at SZA=34.42° (SZA_{Mean}). **(b)** Simulated Reflectance at SZA=36.46° (SZA_{Max}) vs Simulated Reflectance at SZA=34.42° (SZA_{Mean}).

L555: "This commonly known problem" - please add references.

R: Reference is added (Barker and Liu 1995; Page 24, Line 686).

L581ff: How can you be sure the simulation bias is (only or mainly) due to COT? What about effects of further forward model errors (e.g. errors in Reff, PFCT, surface reflection model)

R: We are aware that the 3D effects can affect both cloud optical thickness (COT) and cloud effective radius (Reff; Zhang et al., 2012; Fu et al., 2022). Reff affects the reflectance in two ways: 1) modulating absorption in the shortwave infrared; 2) determining the scattering phase function. Since the simulations is performed for a visible wavelength (650 nm), where cloud do not absorb, the first effect is minimal. The second effect is small because the phase function does not vary significantly with Reff relative to the impact of COT. Therefore, we believe that the reflectance 3D effect is dominated by the cloud optical thickness (COT) distribution is reasonable. From Figure 7 of the manuscript, we can see that a good agreement is achieved for generally low radiance, indicating surface is well-modeled in the simulation.

L607ff: Please add (again?) what the domain size (Nx, Ny, Nz) of this simulation is.

R: The 3D atmosphere of clouds has the dimension of [Nx=1188, Ny=1188, Nz=26] with resolution of [dx=0.25km, dy=0.25km, dz=0.5km], which leads to a (1188, 1188) output of radiance field. We added the clarification in the revised manuscript (Page 26, Line 744).

L644f: What kind of interpolation is used?

R: The used interpolation is linear interpolation (added clarification in Page 27, Line 782).

L669f: Why does a low-biased AHI COT introduce a high bias in IPA-based simulations here, in contrast to APP1?

R: For APP1, the comparison is made for reflectance whereas for AHI, the comparison is made for transmittance. In APP1, the low bias in reflectance indicates low bias in COT. High bias in transmittance, however, indicates low bias in COT (high transmittance is associated with optically thin clouds).

L662f & 700f: Shouldn't the comparison rather be made on the resolution of the input data, ie AHI resolution, ie integrating/averaging SPN-S data? how does it look if that is done?

R: Originally, we thought about two approaches of a) interpolating AHI simulations (3D irradiance field based on AHI cloud retrievals) into aircraft location, and b) integrating/averaging SPN-S data into AHI resolution. We selected method (a) over method (b) because AHI resolution changes (finest at nadir), thus method (a) was easier to implement. We think both methods produce the same results in histograms. As an example, we performed the analysis (integrating/averaging SPN-S data onto AHI resolution) for the flight track shown in Figure 8 of this paper, as indicated in Figure 8-extra (the following figure). First, we evaluated the interpolation effect for the simulations. The red and blue are irradiance simulations linearly interpolated at flight locations, whereas the magenta and cyan shows irradiance simulations closest to the flight locations. From the histograms, we can see the interpolations effects are minimal – no major shifts in histogram despite interpolation offers more continuity. Next, we sampled (binned) the SPN-S data at AHI resolution (gray). After doing that, we saw that the variability decreased (maximum and minimum values) but the histogram shape remained fairly similar.

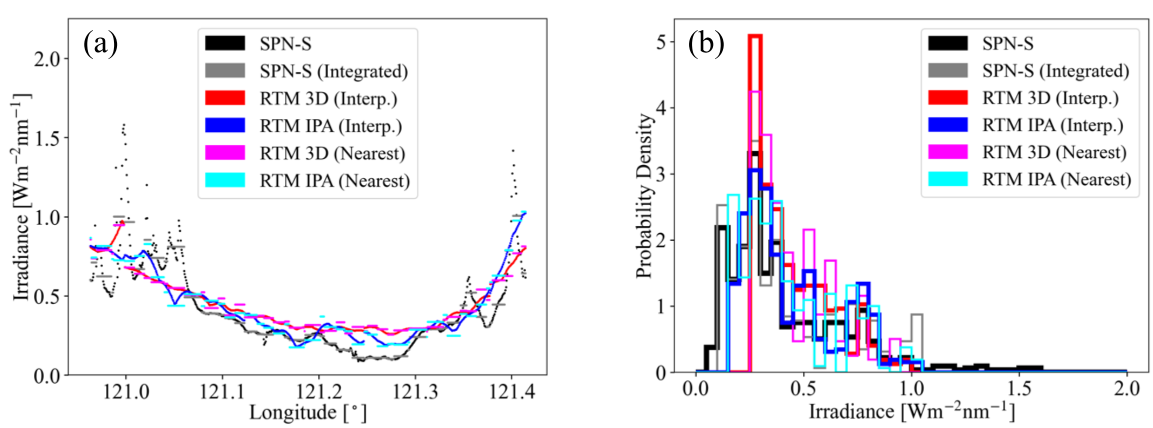

Figure 8-extra: **(a)** The same as Figure 8 in the manuscript except adding SPN-S averaged over AHI resolution grids (in gray), irradiance calculations closest to the flight locations (magenta and cyan) instead of linear interpolation (red and blue). **(b)** Histograms (probability density).

L722f: "We found that the bias [...] is partially caused by the coarse imager resolution" - in my understanding of the manuscript, that is rather a hypothesis. have you tested that somehow (eg by comparing on an AHI resolution basis, averaging/integrating the SPN-S obs to the AHI resolution)?
R: We agree. We added some discussions (Page 30, Line 867) in the revised manuscript. As we mentioned in the response to previous comment, averaging the SPN-S observations to the AHI resolution will not change the distribution of the histogram.

L872ff: "bias [...] was either due" - reformulate. The bias is quite surely not exclusively due to only one of these (as "either" implicates). Those two are very likely two main contributors (as stated above, I think, regarding the role of coarse resolution, this remains a hypothesis so far as in my understanding you have not demonstrated that yet.
R: We meant to state the bias is due to a combination of the two – 1) coarse imagery resolution, and 2) 3D effects. We changed the wording to clarify in the revised manuscript (Page 38, Line 1096).

L686: "their distributions are completely different" - I do not agree at all. Apart from the Trans>1 tail (and the equivalent higher peak in IPA at Trans~0.9, they are fairly similar. Particularly when compared to the observations.
R: We removed "completely" in the revised manuscript (Page 29, Line 838).

Fig9: For my feeling(!), the observations have a surprisingly high amount of Trans>1 (I'd by-eye-guess ~20% of all data). Is that expected, ie is the phenomenon that common?
R: We agreed that the transmittance greater than 1 is in surprisingly frequent, but that is expected. During the CAMP^{2}Ex mission, we saw extremely variable cloud conditions – fast-evolving, cirrus above, ubiquitous small size cumulus humilis clouds (cannot be resolved by geostationary satellite imagery). The phenomenon is expected because of the 3D effects associated with the cumulus ("popcorn") clouds. One point to clarify is that the imagery from the geostationary satellite as shown in Figure 8a does not represent the general cloud conditions for the entire campaign, whereas the histogram provided in Figure 9 does use *all* the below-clouds measurements from the entire CAMP^{2}Ex, not just the flight track shown in Figure 8. To make this point transparent to the reader, we published "flight videos" that we created for most of the research flights during CAMP^{2}Ex in the revised manuscript. This provides a better understanding of the cloud conditions.

Or could other things contribute (like calibration)?
R: The reviewer is correct, the calibration uncertainty can indeed contribute. To evaluate how this can affect the results, we applied a scale factor of 0.93 to the SPN-S measurements, assuming SPN-S consistently took measurements with largest reported calibration uncertainty of 7%. This scaling, however, will result in a 7% low bias of the SPN-S measurements compared to

calculations for the high legs when the aircraft flew at altitudes around 6 – 7 km. We are therefore rather confident that SPN-S's calibration is actually accurate. Still, it is worthwhile looking at the results when scaling SPN-S down to the lower end of its uncertainty range. This is shown in Figure 9-extra below. The down-scaled SPN-S measurements below clouds (green) do show better agreement with the calculations (red) in terms of 1) average values (dashed lines), and 2) the high transmittance peak of the histogram (thin clouds and clear-sky). However, at the low transmittance side of the histogram (below a transmittance of ~0.5, thick clouds), the agreement becomes worse after rescaling, and generally the measured shape of the histogram still differs significantly from that of the calculations. To summarize, the calibration uncertainties can be propagated into the histogram and may affect not only the average values, but also the histogram shape. However, adjusting the calibration within the uncertainty will only lead to better agreement of one aspect at the expense of another. In other words, down-scaling the SPN-S measurements will lead to a better agreement of the campaign-average transmittance, but lead to a low-bias of the measurements above the clouds, and lead to worse agreement on the low-transmittance end below clouds.

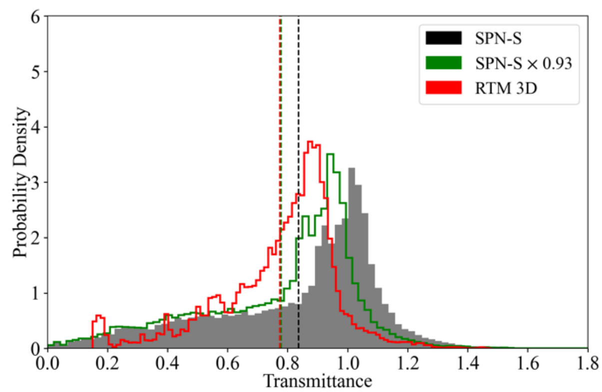

Figure 9-extra: The same as Figure 9 in the manuscript except removing IPA calculations (originally in blue) and adding downscaled SPN-S observations (by a factor of 0.93) in green.

Sec6: I'd like to see some characterizing stats of the CNN, e.g. histograms of COT and/or radiance of training and validation data and retrieval uncertainties for either data subset.

R: We provided some brief descriptions for the CNN in Appendix B (Page 43, Line 1174). The histograms of the COT of the training dataset is provided at Figure 10b in Nataraja et al., 2022 (also see the following figure).

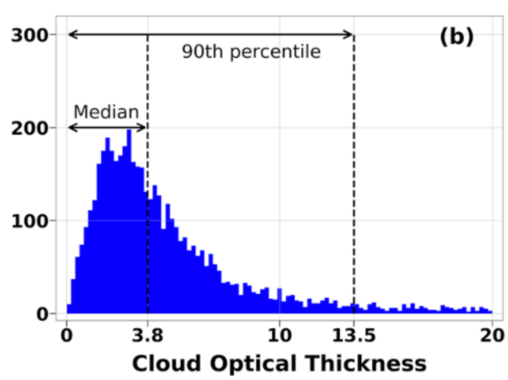

Figure 10b in Nataraja et al., 2022: Histogram of the cloud optical thickness for the sampled dataset used for the CNN training.

L739ff: Does that mean that for more global/operational application, separate CNNs for different SZA(-ranges) would need to be trained (SAA could still be handled by automatized rotation, I assume)? what further work do you see for a more global application?

R: 3D bias mitigation towards global/operational application is indeed an over-arching, but somewhat distant, goal. This paper is just an initial step in offering tools and barebone structures of demo for approaching this problem. We are developing more sophisticated CNN algorithms – testing different CNN techniques, training CNN on various cloud and surface types under different solar conditions, and gradually extend the application to global/operational application. For example, a former postdoc in our group has extended such an application to geostationary satellite imagery. This work is in manuscript stage and will be submitted to AMT in the near-future. Aside from developing more sophisticated and comprehensive CNN algorithms, we are also developing techniques to further accelerate the 3D calculations such as GPU application, hierarchical gridding, etc. so that it becomes operationally feasible for 1) generating large dataset for training CNN and 2) achieving the radiance self-consistency concept proposed in the manuscript at a global scale.

Fig10: Add indicators of the direction of the sun (or of north) in (a). Remove colored dots in (a) and their mentioning in caption when not otherwise explained and used (did i miss that in text?). Is the (6.4km)2 area the one inside the black or the red rectangle in (b), or the circular area? Does the circular are in (b) correspond to the yellow-circled area in (a)? "Inside [...] shown instead" - Formulate more straightforward to ease understanding: Inside the rectangle = regridded obs, circular area outside the rectangle = observed red channel radiance at native image resolution? why is the regridding done specifically to 100m resolution and how? caption refers to solid black lines indicated square area - I can't spot that; missing or badly visible?

R: Figure 10a and 10b are modified (see the following Figure as well as in the revised manuscript) – Figure 10a: removed colored dots and added arrows to indicate true north, flight direction, and sun position; Figure 10b: removed the original red lines and changed the black lines into red for better distinction. After modification, now in the new figures, the red circle in Figure 10a indicates the circular area in Figure 10b; the 6.4×6.4 km^2 region is indicated by red lines in Figure 10b. The boxed area in Figure 10b is the study region, which is gridded into 100 m resolution to match the spatial resolution of the training dataset of CNN. The outside-box area in Figure 10b is shown with native camera resolution but is not used in the study. We modified the text and added clarification (Page 32, Line 924).

(a)

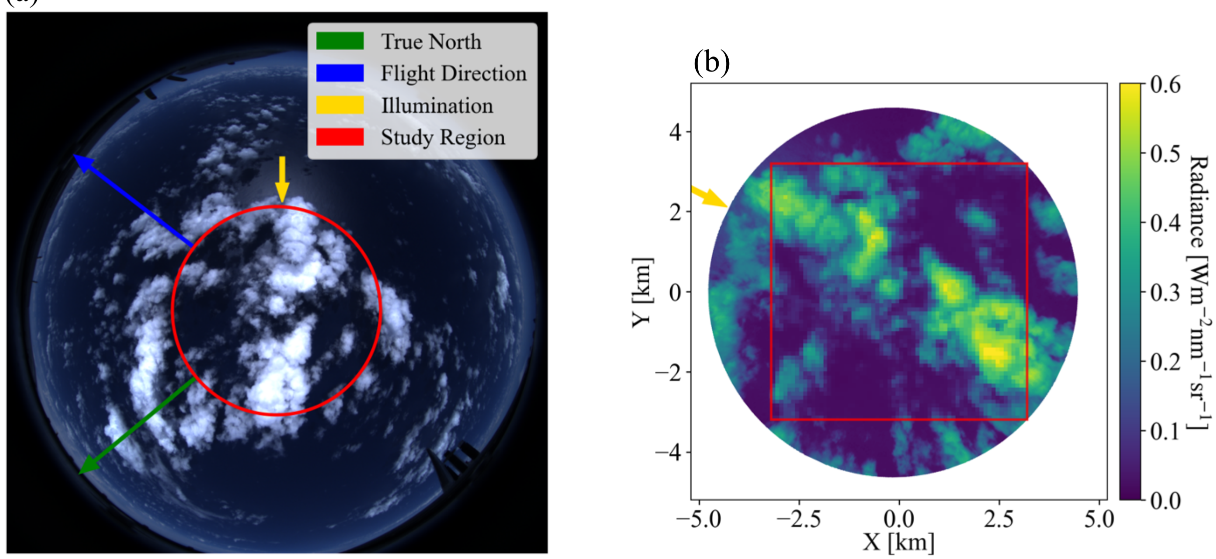

Figure 10. (a) RGB imagery of nadir-viewing all-sky camera deployed during CAMP2Ex for a cloud scene centered at [123.392°E, 15.2744°N] over the Philippine Sea at 02:10:06 UTC on 5 October, 2019. The arrows indicate the true north (green), flight direction (blue), and illumination (where the sunlight comes from, yellow). **(b)** Red channel radiance measured by the camera for the circular area indicated by the red circle in (a). Red squared region shows gridded radiance with a pixel size of 64x64 and spatial resolution of 100 m.

Fig10, Fig12: Please make sure, figure, caption, and text are consistent. Eg. text mentions 12 edge pixels for Fig12, caption 7 on each side.

R: Thank you for noticing the typo. The number of excluded edge pixels should be 7. We corrected the text in the revised manuscript (Page 33, Line 964).

Fig12: Would be nice to have the observation data (red rectangle region) repeated here in the same style as the simulations for easier comparison.

R: We added the measured radiance (Figure 12c) in the same format as simulations for easy comparison (Page 34, Line 990).

Fig13: Reconsider the colors used. black dots on low histogram value colors are badly discernible. why are there dots outside the histrogram colored area? why are there no dots in the low-radiance corner, but histogram colors indicate high density? Is that an interpolation effect of the plotting (better to plot original binned data w/o interplation/smoothing)? Are the data shown from native imagery or regridded image resolution (or mixed???)?

R: We changed the colormap to better distinguish black dots from background color. The dots outside the colored area is due to the color range assigned to the number of occurrence – before, only occurrence greater than 2 were picked up from the background color. We removed the background where no data exists for Figure 13 for better visualization. The low-radiance corner indicates clear-sky to very-thin clouds. Since the surface albedo of the ocean at 600 nm, although very dark, is not zero. Additionally, due to 3D effects (clouds scatter radiation to the clear-sky region), we rarely have a radiance of 0 in neither measurements nor simulations. The interpolation/smoothing is in the visualization but does not have an effect on the distribution. The black dots are the re-gridded data (100m resolution) indicated in Figure 12 and the colored heatmap is the 2D histogram of the data.

Fig14 & discussion (L821-824): First, together with the ambiguous plotting of the mean CRE lines in Fig14a, the formulation of the "minor finding" is not fully clear. Does it mean that meanCRE(COT_CNN) is similar for both IPA and 3D RT simulations, and the same applies for meanCRE(COT_IPA)? I.e. mean of black solid is similar to mean of dashed blue on the one hand and solid red similar to dashed green? That would be in agreement with the following concluding sentence (L823f) and at least with the mean indicating lines in Fig14b (Fig14a I can't judge since the overlap of the lines renders the colors indistinguishable). While I buy that for Fig14b (ie CRE above clouds), from by-eye-judgement, I doubt that for Fig14a (CRE below clouds), since the blue dashed compared to the black solid curve seems to be shifted towards lower CRE (ie I expect mean(blue) < mean(black)) while green dashed compared to solid red seems shifted towards higher CRE (ie I expect mean(green) > mean(red)). Furthermore, in Fig14a both black solid and dashed green on the one hand as well as red solid and blue dashed on the other are very similar to each other (ie the two IPA and the two 3D RT simulations, respectively, regardless of COT retrieval method) - in both shape (that is, regardless of any other issues, regarding below-cloud CRE I dont not agree with your L823 statement that the PDFs are very dissimilar) and location along the CRE axis. Is there anything wrong, maybe, with the color coding of either the PDFs or the mean indication lines? Please check color coding and your respective conclusions.
R: Thank you for your comments. We modified the Figure 14 to make the different colored lines more distinguishable (we changed the black lines into gray lines and increased the line thickness). Yes, we meant $\overline{CRE_{IPA}(COT_{CNN})} \approx \overline{CRE_{3D}(COT_{CNN})}$ (blue dashed line overlay gray solid line) and $\overline{CRE_{IPA}(COT_{IPA})} \approx \overline{CRE_{3D}(COT_{IPA})}$(green dashed line overlay red solid line). We added clarification in the revised manuscript (Page 36, Line 1037). We understood the conclusion is counter-intuitive but can be explained. For example, for Figure 14a, let's stick with $CRE_{3D}(COT_{CNN})$ (gray) and $CRE_{IPA}(COT_{CNN})$ (blue). The $CRE_{IPA}(COT_{CNN})$ (blue) has a more symmetric PDF distribution, thus the mean (blue dashed line) is located at the middle of the PDF. The $CRE_{3D}(COT_{CNN})$ (gray), however, has a gamma-like distribution – most of the CRE are very-negative, thus the mean (gray solid line) locates closer to the where the PDF is peaked. Thus, even though the histogram looks shifted to the right from blue to gray, their averages are similar.

L904: Over what data is that median taken? The processed scene? Does that work satisfactorily, e.g. over bright surfaces like deserts or snow covered areas?
R: The median is taken over the processed scene. It works satisfactorily for the given scene but will undoubtedly fail for scenes with less contrast, e.g., clouds over bright surfaces in the Arctic. Again, the applications demonstrated in this paper aim at providing bare-bone structure of approach for addressing well-known problems in 3D radiation science. A few more robust and universal cloud detection/mask algorithms are under development within our group, e.g., utilize multi-angle observations and/or information of scene variance in addition to scene brightness. Such algorithms will be discussed in future papers by Yu-Wen Chen (graduate student in our group)

et al., which applies the EaR^3T to improve CO_2 retrievals for OCO-2 (extended work from App. 1).

Technical corrections

C: Fig1: Make the figure larger (e.g., in landscape orientation) to make it better readable. Add color coding info to the caption.
R: We modified the figure into landscape orientation and added legend for color coding (Page 7, Line 182).

C: L203: "includes Monte" -> "includes the Monte"
R: We changed to "includes MCARaTS" (Page 9, Line 244).

C: L267: Are only channels 1 and 2 of MODIS L1B product used? Please specify their wavelengths here.
R: Yes, you are correct. We added wavelength information for clarification (see Page 13, Line 330).

C: L313: A reference to the correction effect figure in Appendix B would be useful.
R: Reference added (see Page 14, Line 394).

C: L486f: I am unsure what the documentation sentence here is supposed to tell the reader. Maybe it's just that the "only" is out of place here? However, there no other mention of (further) documentation elsewhere in the text, so this seems odd here.
R: We changed the wording and moved the sentence to the end of Section 2.1 (see Page 11, Line 282).

C: L531: "scale the MYD09 field" - Please add, which parameter this refers to (surface albedo/reflectance, I assume).
R: Yes, you are correct, we added "surface reflectance" for clarification (see Page 22, Line 651).

C: Fig8a: The flight track line is hardly visible; make it thicker. Caption misses an explanation what the thin and thick line sections are.
R: We made the lines thicker for better visibility and added explanation for the thin and thick lines (see Page 29, Line 824).

C: Fig9: "Vice versa for the green" - Misleading formulation. Like for yellow, PD(obs)>PD(sim) here, not PD(obs)<PD(sim) as "vice versa" implies.
R: We changed the wording to make it rigorous (see Page 30, Line 848).

C: L699: "the simulation histogram peaks" -> "the simulation histograms peak"
R: Corrected (see Page 30, Line 853).

C: L728: "use a high-resolution imagery" - remove "a"
R: Corrected (see Page 31, Line 894).

C: L801f: "By contrast" -> "In contrast"
R: Corrected (see Page 35, Line 1013).

C: Fig14: Please use larger font in legend for improved readability. Find a better way to indicate the overlapping mean-value lines - it's indiscernible which of the dashed lines lies where, particularly in (a).
R: We increased the font size for the legend. Additionally, we changed black lines to gray lines for better distinction (see Page 36, Line 1045).

C: L887: "introduce a warming bias" - I rather suggest "warm bias"; with CRE<0 the term "warming" feels odd.
R: We adapted the change (see Page 38, Line 1110).

C: L946: "in the black box" -> rather "in the inset"? (equivalently at L952)
R: We adapted the change (see Page 46, Line 1238 and Page 47, 1262).

C: L1093ff: Add info where to you intend to submit Schmidt et al., 2022 (same Special Issue?)
R: Schmidt et al. 2022 will be submitted AMT but not to the CAMP^{2}Ex special issue. We added clarification for the reference (… to be submitted to Atmos. Meas. Tech. …) in the revised manuscript (Page 54, Line 1475).

References:

Barker, H. W., Jerg, M. P., Wehr, T., Kato, S., Donovan, D. P., and Hogan, R. J.: A 3D cloud construction algorithm for the EarthCARE satellite mission, Q. J. Roy. Meteor. Soc., 137, 1042– 1058, https://doi.org/10.1002/qj.824, 2011.

Fu, D., Di Girolamo, L., Rauber, R. M., McFarquhar, G. M., Nesbitt, S. W., Loveridge, J., Hong, Y., van Diedenhoven, B., Cairns, B., Alexandrov, M. D., Lawson, P., Woods, S., Tanelli, S., Schmidt, S., Hostetler, C., and Scarino, A. J.: An evaluation of the liquid cloud droplet effective radius derived from MODIS, airborne remote sensing, and in situ measurements from CAMP2Ex, Atmos. Chem. Phys., 22, 8259–8285, https://doi.org/10.5194/acp-22-8259-2022, 2022.

Nataraja, V., Schmidt, S., Chen, H., Yamaguchi, T., Kazil, J., Feingold, G., Wolf, K., and Iwabuchi, H.: Segmentation-Based Multi-Pixel Cloud Optical Thickness Retrieval Using a Convolutional Neural Network, Atmos. Meas. Tech., 15, 5181–5205, doi:10.5194/amt-15-5181-2022, 2022.

Zhang, Z., Ackerman, A. S., Feingold, G., Platnick, S., Pincus, R., and Xue, H.: Effects of cloud horizontal inhomogeneity and drizzle on remote sensing of cloud droplet effective radius: Case studies based on large-eddy simulations, J. Geophys. Res.-Atmos., 117, D19208, https://doi.org/10.1029/2012jd017655, 2012.

The Education and Research 3D Radiative Transfer Toolbox (EaR^{3}T) – Towards the Mitigation of 3D Bias in Airborne and Spaceborne Passive Imagery Cloud Retrievals

Hong Chen[1,2], K. Sebastian Schmidt[1,2], Steven T. Massie[2], Vikas Nataraja[2], Matthew S. Norgren[2], Jake J. Gristey[3,4], Graham Feingold[4], Robert E. Holz[5], Hironobu Iwabuchi[6]

[1]Department of Atmospheric and Oceanic Sciences, University of Colorado, Boulder, CO, USA
[2]Laboratory for Atmospheric and Space Physics, University of Colorado, Boulder, CO, USA
[3]Cooperative Institute for Research in Environmental Sciences, University of Colorado, Boulder, CO, USA
[4]NOAA Chemical Sciences Laboratory, Boulder, CO, USA
[5]Space Science and Engineering Center, University of Wisconsin–Madison, Madison, WI, USA
[6]Center for Atmospheric and Oceanic Studies, Tohoku University, Sendai, Miyagi, Japan

Correspondence to: Hong Chen (hong.chen-1@colorado.edu)

Abstract

We introduce the Education and Research 3D Radiative Transfer Toolbox (EaR^{3}T) for quantifying and mitigating artifacts in atmospheric radiation science algorithms due to spatially inhomogeneous clouds and surfaces, and show the benefits of automated, realistic radiance and irradiance generation along extended satellite orbits, flight tracks from entire aircraft field missions, and synthetic data generation from model data. EaR^{3}T is a modularized Python package that provides high-level interfaces to automate the process of 3D radiative transfer (RT) calculations. After introducing the package, we present initial findings from four applications, which are intended as blueprints to future in-depth scientific studies. The first two applications use EaR^{3}T as a satellite radiance simulator for the NASA Orbiting Carbon Observatory 2 (OCO-2) and Moderate Resolution Imaging Spectroradiometer (MODIS) missions, which generate synthetic satellite observations with 3D-RT on the basis of cloud field properties from imagery-based retrievals and other input data. In the case of inhomogeneous cloud fields, we show that the synthetic radiances are often inconsistent with the original radiance measurements. This lack of radiance consistency points to biases in heritage imagery cloud retrievals due to sub-pixel resolution clouds and 3D-RT effects. They come to light because the simulator's 3D-RT engine replicates processes in nature that conventional 1D-RT retrievals do not capture. We argue that 3D radiance consistency (closure) can serve as a metric for assessing the performance of a cloud retrieval in presence of spatial cloud inhomogeneity even with limited independent validation data. The other two applications show how airborne measured irradiance data can be used to independently validate imagery-derived cloud products via radiative closure in irradiance. This is accomplished by simulating downwelling irradiance from geostationary cloud retrievals of Advanced Himawari Imager (AHI) along all the below-cloud aircraft flight tracks of the Cloud, Aerosol and Monsoon Processes Philippines Experiment (CAMP^{2}Ex, NASA 2019), and comparing the irradiances with the collocated airborne measurements. In contrast to isolated case studies in the past, EaR^{3}T facilitates the use of observations from entire field campaigns for the statistical validation of satellite-derived irradiance. From the CAMP^{2}Ex mission, we find a low bias of 10% in the satellite-derived cloud transmittance, which we are able to attribute to a combination of the coarse resolution of the geostationary imager and 3D-RT biases. Finally, we apply a recently developed context-aware Convolutional Neural Network (CNN) cloud retrieval framework to high-resolution airborne imagery from CAMP^{2}Ex and show that the retrieved cloud optical thickness fields lead to better 3D radiance consistency than the heritage independent pixel algorithm, opening the door to future mitigation of 3D-RT cloud retrieval biases.

1. Introduction

Three-dimensional cloud effects in imagery-derived cloud properties have long been considered an unavoidable error source when estimating the radiative effect of clouds and aerosols. Consequently, research efforts involving satellite, aircraft, and surface observations in conjunction with modeled clouds and radiative transfer calculations have focused on systematic bias quantification under different atmospheric conditions. Barker and Liu (1995) studied the so-called independent pixel approximation (IPA) bias in cloud optical thickness (COT) retrievals from shortwave cloud reflectance. The bias arises when approximating the radiative transfer relating to COT and measured reflectance at the pixel or cloud column level through one-dimensional (1D) radiative transfer (RT) calculations, while ignoring its radiative context. However, net horizontal photon transport and other effects such as shading engender column-to-column radiative interactions that can only be captured in a three-dimensional (3D) framework, and can be regarded as a 3D perturbation or bias relative to the 1D-RT (IPA) baseline. 3D biases affect not only cloud remote sensing but they also propagate into the derived irradiance fields and cloud radiative effects (CRE). Since the derivation of regional and global CRE relies heavily on satellite imagery, any systematic 3D bias impacts the accuracy of the Earth's radiative budget. Likewise, imagery-based aerosol remote sensing in the vicinity of clouds can be biased by net horizontal photon transport (Marshak et al., 2008). Additionally, satellite shortwave spectroscopy retrievals of CO_2 mixing ratio are affected by nearby clouds (Massie et al., 2017), albeit through a different physical mechanism than in aerosol and cloud remote sensing (Schmidt et al., 2022).

Given the importance of 3D perturbations for atmospheric remote sensing, ongoing research seeks to mitigate the 3D effects. Cloud tomography, for example, inverts multi-angle radiances to infer the 3D cloud extinction distribution (Levis et al., 2020). This is achieved through iterative adjustments to the cloud field until the calculated radiances match the observations. Convolutional neural networks (CNNs, Masuda et al., 2019; Nataraja et al., 2022) account for 3D-RT perturbations in COT retrievals through pattern-based machine learning that operates on collections of imagery pixels, rather than treating them in isolation like IPA. Unlike tomography, CNNs require training based on extensive cloud-type specific synthetic data with the ground truth of cloud optical properties and their associated radiances from 3D-RT calculations. Once the CNNs are trained, they do not require real-time 3D-RT calculations and can therefore be useful in an operational setting. Whatever the future may hold for context-aware multi-pixel or multi-sensor cloud retrievals, there is a paradigm shift on the horizon that started when the radiation concept for the Earth Clouds, Aerosol and Radiation Explorer (EarthCARE, Illingworth et al., 2015) was first proposed (Barker et al., 2012). It foresees a closure loop where broadband radiances, along with irradiance, are calculated in a 3D-RT framework from multi-sensor input fields (Barker et al., 2011), and subsequently compared to independent observations by radiometers pointing in three directions (nadir, forward-, and backward-viewing along the orbit). This built-in radiance closure can serve as an accuracy metric for any downstream radiation products such as heating rates and CRE. Any inconsistencies can be used to nudge the input fields towards the truth in subsequent loop iterations akin to optimal estimation, or propagated into uncertainties of the cloud and radiation products.

This general approach to radiative closure is also being considered for the National Aeronautics and Space Administration (NASA) Atmospheric Observation System (AOS, developed under the A-CCP, Aerosol and Cloud, Convection and Precipitation study), a mission that is currently in its early implementation stages. Owing to its focus on studying aerosol-cloud-precipitation-radiation interactions at the process level, it requires radiation observables at a finer spatial resolution than achieved with missions to date. At target scales close to 1 km, 3D-RT effects are much more pronounced than at the traditional 20 km scale of NASA radiation products (O'Hirok and Gautier, 2005; Ham et al., 2014; Song et al., 2016; Gristey et al., 2020a). Since this leads to biases beyond the desired accuracy of the radiation products, mitigation of 3D-RT cloud remote sensing biases needs to be actively pursued over the next few years.

Transitioning to an explicit treatment of 3D-RT in operational approaches entails a new generation of code architectures that can be easily configured for various instrument constellations, interlink remote sensing parameters with irradiances, heating rates, and other radiative effects, and can be used for automated processing of large data quantities. A number of 3D solvers are available for different purposes, for example, the I3RC (International Intercomparison of 3D Radiation Codes: Cahalan et al., 2005) community Monte Carlo code[1], which now also includes an online simulator[2] (Gatebe et al., 2021); MCARaTS (Monte Carlo Atmospheric Radiative Transfer Simulator[3]: Iwabuchi, 2006); MYSTIC (Monte Carlo code for the physically correct tracing of

[1] https://earth.gsfc.nasa.gov/climate/model/i3rc, last accessed on 26 November, 2022.
[2] http://i3rcsimulator.umbc.edu, last accessed on 26 November, 2022.
[3] https://sites.google.com/site/mcarats/monte-carlo-atmospheric-radiative-transfer-simulator-mcarats, last accessed on 26 November, 2022.

photons in cloudy atmospheres: Mayer, 2009), which is embedded in libRadtran (library for radiative transfer, Mayer and Kylling, 2005); McSCIA (Monte Carlo [RT] for SCIAmachy: Spada et al., 2006), which is optimized for satellite radiance simulations (including limb-viewing) in a spherical atmosphere; McARTIM (Deutschmann et al., 2011), with several hyperspectral polarimetric applications such as differential optical absorption spectroscopy; and SHDOM (Spherical Harmonic Discrete Ordinate Method[4]: Evans, 1998), which, unlike the other methods, is a deterministic solver with polarimetric capabilities (Doicu et al., 2013; Emde et al., 2015) that is differentiable and can therefore be used for tomography (Loveridge et al., 2022).

For the future operational application of 3D-RT, it is, however, desirable to run various different solvers in one common architecture that automates the processing of various formats of 3D atmospheric input fields (including satellite data), allows the user to choose from various options for atmospheric absorption and scattering, and simulates radiance and irradiance data for real-world scenes. Here, we introduce one such tool that could serve as the seed for this architecture: the Education and Research 3D Radiative Transfer Toolbox (EaR^{3}T). It has been developed over the past few years at the University of Colorado to automate 3D-RT calculations based on imagery or model cloud fields with minimal user input. EaR^{3}T is maintained and extended by graduate students as part of their education, and applied to various different research projects including machine learning for atmospheric radiation and remote sensing (Gristey et al., 2020b; 2022; Nataraja et al., 2022), as well as radiative closure and satellite simulators (this paper and Schmidt et al., 2022). It is implemented as a modularized Python package with various application codes that combine the functionality in different ways, which, once set up, autonomously process large amounts of data required by airborne and satellite remote sensing and for machine learning applications.

Deleted: transition

The goal of the paper is to introduce EaR^{3}T as a versatile tool for systematically quantifying and mitigating 3D cloud effects in radiation science as foreseen in future missions. To do so, we will first showcase EaR^{3}T as an automated radiance simulator for two satellite instruments, the Orbiting Carbon Observatory-2 (OCO-2, this application is referred to as App. 1 in this manuscript) and the Moderate Resolution Imaging Spectroradiometer (MODIS, application code 2, App. 2) from publicly available satellite retrieval products. In the spirit of radiance closure, the intended use is the comparison of modeled radiances with the original measurements to assess the accuracy

Deleted: APP1

Deleted: APP

[4] https://coloradolinux.com/shdom, last accessed on 26 November, 2022.

of the input data, as follows: operational IPA COT products are made using 1D-RT, and thus the accompanying radiances are consistent with the original measurements under that 1D-RT assumption only. That is, self-consistency is assured if 1D-RT is used in both the inversion and radiance simulation. However, since nature creates 3D-RT radiation fields, we break this traditional symmetry in this manuscript and introduce the concept of 3D radiance consistency where closure is only achieved if the original measurements are consistent with the 3D-RT (rather than the 1D-RT) simulations. The level of inconsistency is then used as a metric for the magnitude of 3D-RT retrieval artifacts as envisioned by the architects of the EarthCARE radiation concept (Barker et al., 2012).

Deleted: operates

Deleted: on

Subsequently, we discuss applications where EaR^{3}T performs radiative closure in the traditional sense, i.e., between irradiances derived from satellite products and collocated airborne or ground-based observations. The aircraft Cloud, Aerosol and Monsoon Processes Philippines Experiment (CAMP^{2}Ex, Reid et al., 2022), conducted by NASA in the Philippines in 2019, serves as a testbed of this approach. Here, we use EaR^{3}T's automated processing capabilities to derive irradiance from geostationary imagery cloud products and then compare these to cumulative measurements made along all flight legs of the campaign (application code 3, App. 3). In contrast to previous studies that often rely on a number of cases (e.g., Schmidt et al., 2010; Kindel et al., 2010), we perform closure systematically for the entire data set, enabling us to identify 3D-RT biases in a statistically significant manner. Finally, we apply a regionally and cloud type specific CNN, introduced by Nataraja et al. (2022) that is included with the EaR^{3}T distribution, to high-resolution camera imagery from CAMP^{2}Ex. This last example demonstrates mitigation of 3D-RT biases in cloud retrievals using the concept of radiance closure to quantify its performance against the baseline IPA (application code 4).

Deleted: APP

The general concept of EaR^{3}T with an overview of the applications, along with the data used for both parts of the paper is presented in section 2, followed by a description of the procedures of EaR^{3}T in section 3. Results for the OCO-2 and MODIS satellite simulators (part 1) are shown in section 4, followed by the quantification and mitigation of 3D-RT biases with CAMP^{2}Ex data in section 5 and section 6 (part 2). A summary and conclusion are provided in section 7. The code, along with the applications presented in this paper, can be downloaded from the GitHub repository: https://github.com/hong-chen/er3t.

Deleted: github

2. Functionality and Data Flow within EaR^{3}T

2.1 Overview

To introduce EaR^{3}T as a satellite radiance simulator tool and to demonstrate its use for the quantification and mitigation of 3D cloud remote sensing biases, five applications (Figure 1) are included in the GitHub software release, four of which are discussed in this paper:

Deleted: github

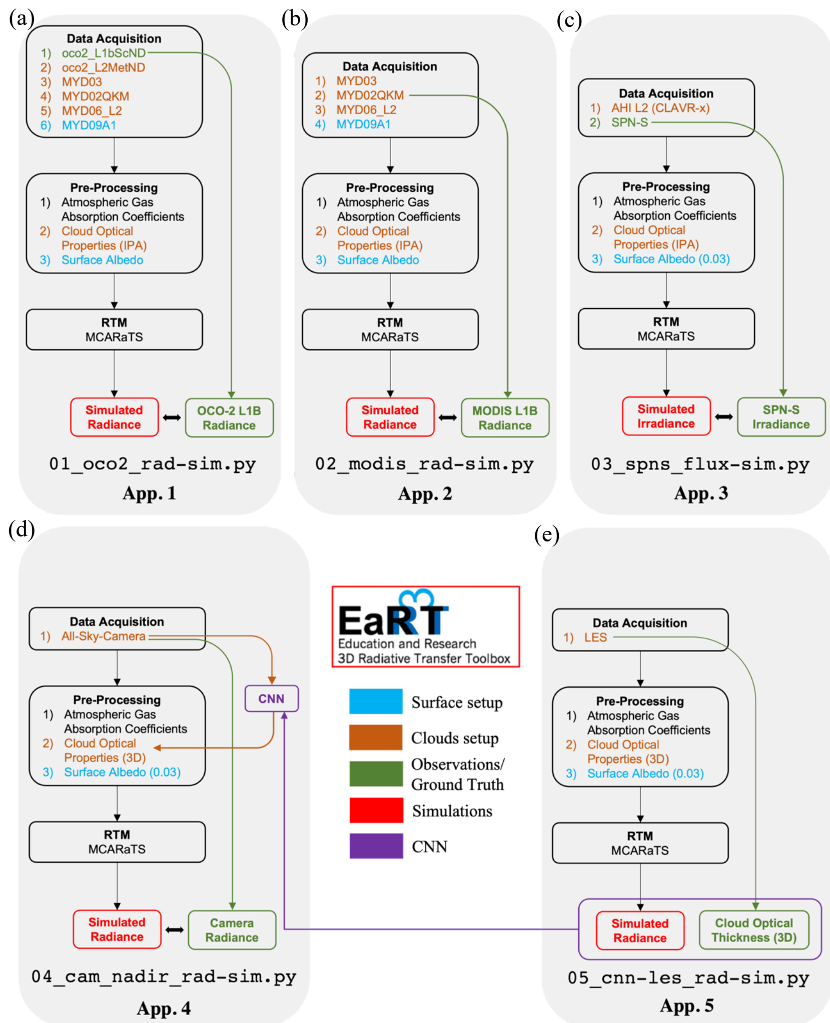

Figure 1. Flow charts of EaR^{3}T applications for (a) OCO-2 radiance simulation at 768.52 nm (data described in section 2.2.1 and 2.2.2, results discussed in section 4), (b) MODIS radiance simulation at 650 nm (data described in section 2.2.1, results discussed in section 4), (c) SPN-S irradiance simulation at 745 nm (data described in section 2.2.3 and 2.2.4, results discussed in section 5), (d) all-sky camera radiance simulation at 600 nm (data described in section 2.2.5, results discussed in section 6), and (e) radiance simulation at 600 nm based on LES data for CNN training (Appendix B). The data products and their abbreviations are described in section 2.2.

Deleted: not included in this paper

1. App. 1, section 4.1 (`examples/01_oco2_rad-sim.py`): Radiance simulations along the track of OCO-2, based on data products from MODIS and others – to assess consistency (closure) between simulated and measured radiance;
2. App. 2, section 4.2 (`examples/02_modis_rad-sim.py`): MODIS radiance simulations – to assess self-consistency of MODIS level-2 (L2) products with the associated radiance fields (L1B product) under spatially inhomogeneous conditions;
3. App. 3, section 5 (`examples/03_spns_flux-sim.py`): Irradiance simulations along aircraft flight tracks, utilizing the L2 cloud products of the AHI, and comparison with aircraft measurements – to quantify retrieval biases due to 3D cloud structure based with data from an entire aircraft field campaign;
4. App. 4, section 6 (`examples/04_cam_nadir_rad-sim.py`): Mitigation of 3D cloud biases in passive imagery COT retrievals from an airborne camera, application of a convolutional neural network (CNN) and subsequent comparison of CNN-derived radiances with the original measurements – to illustrate how the radiance self-consistency concept assesses the fidelity of cloud retrievals.
5. App. 5, Appendix B (`examples/05_cnn-les_rad-sim.py`): Generation of training data for the CNN (App. 4) based on LES inputs. The training datasets contains 1) the ground truth of COT from the LES data; 2) realistic radiance simulated by EaR^{3}T based on the LES cloud fields.

Deleted: APP

Deleted:

Deleted: APP

Deleted: APP

Deleted:

Deleted: APP

Figure 1 shows the high-level workflow of the applications. The first four share the general concept of evaluating simulations (the output from the EaR^{3}T, indicated in red at the bottom of each column) with observations (indicated in green at the bottom) from various satellite and aircraft instruments. The results for the first four applications are interpreted in section 4.1, section 4.2, section 5, and section 6. The results for App. 5 are discussed in detail in a separate paper by

Nataraja et al. (2022). In this paper, we will only provide a brief description for App. 5 in Appendix B. The workflow of each application consists of three parts – 1) data acquisition, 2) pre-processing, and 3) RTM setup and execution. EaR^{3}T includes functions to ingest data from various different sources, e.g., satellite data from publicly available data archives, which can be combined in different ways to accommodate input data depending on the application specifics. For example, in App. 1, EaR^{3}T is used to automatically download and process MODIS and OCO-2 data files based on the user-specified region, date and time. Building on the templates provided in the current code distribution, the functionality can be extended to new spaceborne or airborne instruments. The fifth column of Figure 1 shows an application that differs from the first four, and was developed for earlier papers (Gristey et al., 2020a and 2020b; Nataraja et al., 2022; Gristey et al., 2022). In contrast to the first four, which use imagery products as input, the fifth application ingests model output from a Large Eddy Simulation (LES) and produces irradiance data for surface energy budget applications, or synthetic radiance fields for training a CNN. Details and results are described in the respective papers. Furthermore, Schmidt et al. (2022) builds upon App. 1 to study the mechanism of 3D cloud biases in OCO-2 passive spectroscopy retrievals.

After the required data files have been downloaded in the data acquisition step, EaR^{3}T pre-processes them and generates the optical properties of atmospheric gases, clouds, aerosols, and the surface. In Figure 1, the mapping from input data to these properties is color-coded component-wise (brown for associated cloud property processing if available, blue for associated surface property processing if available, green for associated ground truth property). The version used in this paper (v0.1.0; Chen and Schmidt, 2022) only includes MCARaTS as the 3D RT solver, but others are planned for the future. MCARaTS is a radiative transfer solver uses Monte Carlo photon-tracing method (Iwabuchi, 2006). It outputs radiation (radiance or irradiance) based on the inputs of radiative properties of surface and atmospheric constituents (e.g., gases, aerosols, clouds) such as single scattering albedo, scattering phase function, or asymmetry parameters, along with solar and sensor viewing geometries. The setup of these input properties is implemented in EaR^{3}T's pre-processing steps, which translates atmospheric properties into solver-specific input with minimum user intervention. To achieve this, EaR^{3}T is modular so that it can be extended as new solvers are added. Although the five specific applications in this paper do not include aerosol layers, the setup of aerosol fields is fully supported and has been used in other applications (e.g., Gristey et al., 2022). After pre-processing, the optical properties are fed into the RT solver. Finally,

Deleted: APP

Deleted: APP

Deleted: -

Deleted: -

Deleted: Although the

Deleted: current

Deleted: the Monte Carlo Atmospheric Radiative Transfer Simulator (…

Deleted: , Iwabuchi, 2006)

Deleted: ,

the user obtains radiation output from EaR^{3}T, either radiance or irradiance. The output is saved in HDF5 format and can be easily distributed and accessed by various programming languages. The data variables contained in the HDF5 output are provided in Table 1.

Metadata			
Variable Name	Description	Data Type	Dimension
`mean/N_photon`	Number of photons per run	Array	N_g
`mean/N_run`	Number of runs	Integer value	N/A
`mean/toa`	TOA downwelling flux	Float value	N/A
Radiance			
Variable Name	Description	Data Type	Dimension
`mean/rad`	Radiance field at user specified altitude averaged over different runs	Array	(N_x, N_y)
`mean/rad_std`	Standard deviation of the radiance fields from different runs	Array	(N_x, N_y)
Irradiance			
Variable Name	Description	Data Type	Dimension
`mean/f_down`	Downwelling irradiance averaged over different runs	Array	(N_x, N_y, N_z)
`mean/f_down_std`	Standard deviation of the downwelling irradiance from different runs	Array	(N_x, N_y, N_z)
`mean/f_down_diffuse`	Diffuse downwelling irradiance averaged over different runs	Array	(N_x, N_y, N_z)
`mean/f_down_diffuse_std`	Standard deviation of the diffuse downwelling irradiance from different runs	Array	(N_x, N_y, N_z)

`mean/f_down_direct`	Direct downwelling irradiance averaged over different runs	Array	(N_x, N_y, N_z)
`mean/f_down_direct_std`	Standard deviation of the direct downwelling irradiance from different runs	Array	(N_x, N_y, N_z)
`mean/f_up`	Upwelling irradiance averaged over different runs	Array	(N_x, N_y, N_z)
`mean/f_up_std`	Standard deviation of the upwelling irradiance from different runs	Array	(N_x, N_y, N_z)

Table 1: Data variables contained in the output HDF5 file from EaR^{3}T for radiance and irradiance calculations. The radiance is simulated with a user-specified sensor geometry at a given altitude using forward photon tracing. The data variables listed under Metadata are included for both radiance and irradiance calculations. N_x, N_y, and N_z are the number of pixels along x, y, and z direction, respectively. N_g is the number of g, explained in section 3 – Correlated-k.

The aforementioned three steps – data acquisition, pre-processing, and RTM setup and execution are automated such that the 3D/1D-RT calculations can be performed for any region at any date and time using satellite or aircraft data or other data resources such as LES. EaR^{3}T is hosted on GitHub at https://www.github.com/hong-chen/er3t. Since it is developed as an educational and research 3D-RT tool collection by students, it is a living code base, intended to be updated over time. The master code modules for the five applications as listed in Figure 1 are included in the EaR^{3}T package under the `examples` directory. In the current release (v0.1.0), only a limited documentation for the installation and usage, including example codes for EaR^{3}T, are provided. More effort will be dedicated for documentation in the near-future.

Deleted: Github

Deleted: four

2.2 Data

The radiance simulations in App. 1 and App. 2 use data from the OCO-2 and MODIS Aqua instruments, both of which are in a sun-synchronous polar orbit with an early-afternoon equator crossing time within NASA's A-Train satellite constellation. Figure 2 visualizes radiance measurements by OCO-2 in the context of MODIS Aqua imagery over a partially vegetated and

Deleted: APP

Deleted: APP

Deleted: -

Deleted:

partially cloud-covered land, illustrating that MODIS provides imagery and scene context for OCO-2, which in turn observes radiances from a narrow swath. The region is located in southwest Colorado in the United States of America. We selected this case because both the surface and clouds are varied along with diverse surface types. The surface features green forest and brown soil, whereas clouds include small cumulus and large cumulonimbus. In addition, this scene contains relatively homogeneous cloud fields in the north and inhomogeneous cloud fields in the south, which allows us to evaluate the simulations from various aspects of cloud morphology. To simulate the radiances of both instruments we use data products from OCO-2 and MODIS, as well as reanalysis products from NASA's Global Modeling and Assimilation Office (GMAO) sampled at OCO-2 footprints and distributed along with OCO-2 data (section 2.2.2).

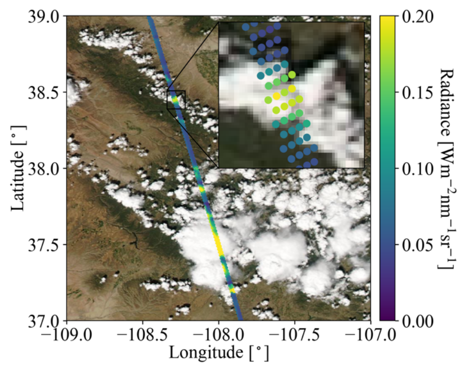

Figure 2. OCO-2 measured radiance (units: $Wm^{-2}nm^{-1}sr^{-1}$) at 768.52 nm, overlaid on MODIS Aqua RGB imagery over southwestern Colorado (USA) on 2 September, 2019. The inset shows an enlarged portion along the track, illustrating that OCO-2 radiances co-vary with MODIS-Aqua radiance observations.

For App. 3 (irradiance simulations and 3D cloud bias quantification), we use geostationary imagery from the Japanese Space Agency's Advanced Himawari Imager to provide cloud information in the area of the flight path of the NASA CAMP^{2}Ex aircraft (Reid et al., 2022). The AHI data are used in conjunction with aircraft measurements of shortwave spectral radiation (section 2.2.4). Subsequently (App. 4: 3D cloud bias mitigation), we demonstrate the concept of radiance closure under partially cloudy conditions with airborne camera imagery (section 2.2.5). The underlying cloud retrieval is based on a convolutional neural network (CNN), which is

Deleted: APP

Deleted: APP

described in a related paper (Nataraja et al., 2022) in this special issue and relies on EaR^{3}T-generated synthetic radiance data based on Large Eddy Simulations (LES).

2.2.1 Moderate Resolution Imaging Spectroradiometer (MODIS)

The MODIS instruments are multi-use multispectral radiometers onboard NASA's Terra and Aqua satellites, which were launched in 1999 and 2002 respectively. MODIS was conceived as a central element of the Earth Observing System (EOS, King and Platnick, 2018). For App. 1 and App. 2, EaR^{3}T ingests MODIS level 1B radiance products at the quarter kilometer scale (channels 1 and 2, bands centered at 650 and 860 nm), MxD02QKM, where 'x' stands for 'O' in the case of MODIS on Terra, and 'Y' in the case of Aqua data), the geolocation product (MxD03), the level 2 cloud product (MxD06), and the surface reflectance product (MxD09A1). For this paper, we use only Aqua data (MYD), from data collection 6.1. All the data are publicly available, and are distributed at the LAADS (Level-1 and Atmosphere Archive & Distribution System) Distributed Active Archive Center (DAAC) by NASA's Goddard Space Flight Center.

For cloud properties in App. 2, we use the MODIS cloud product (MxD06L2, collection 6.1). It provides cloud properties such as cloud optical thickness (COT), cloud effective radius (CER), cloud thermodynamic phase, cloud top height (CTH), etc. (Nakajima and King, 1990; Platnick et al., 2003). Since 3D cloud effects such as horizontal photon transport are most significant at small spatial scales (e.g., Song et al., 2016), we use the high-resolution red (650 nm) channel 1 (250 m), and derive COT directly from the reflectance in the Level-1B data (MYD02QKM) instead of using the coarser-scale operational product from MYD06. CER and CTH are sourced from MYD06 and re-gridded to 250 m. The EaR^{3}T strategy for MODIS data is similar, in principle, to the more advanced method by Deneke et al. (2021), which uses a high resolution wide-band visible channel from geostationary imagery to up-sample narrow-band coarse-resolution channels. However, we simplified cloud detection and derivation of COT from reflectance data for the purpose of our paper by using a threshold method (Appendix C1) and the two-stream approximation (Appendix C2). In future versions of EaR^{3}T this will be upgraded to more sophisticated algorithms. A simple algorithm (Appendix D1) is used to correct for the parallax shift based on the sensor geometries and cloud heights. The cloud top height data is provided by the MODIS L2 cloud product and assuming cloud base is the same.

Deleted: is currently flying
Deleted: on
Deleted: They
Deleted: The
Deleted: are
Deleted: is
Deleted: multi-use multispectral radiometers
Deleted: s
Deleted: APP
Deleted: APP
Deleted: (
Deleted: APP
Deleted: -
Deleted: A1
Deleted: A2
Deleted: B1

For the surface albedo required by the RTM, we used MYD09A1, which provides cloud-cleared surface reflectance observations aggregated over an 8-day period (Vermote et al., 2015). This product is available on a sinusoidal grid with a spatial resolution of 500 m for MODIS band 2, and includes atmospheric correction for gas and aerosol scattering and absorption. Assuming a Lambertian surface in this first release of EaR^{3}T, we used surface reflectance as surface albedo input to the RTM.

2.2.2 Orbiting Carbon Observatory 2 (OCO-2)

The OCO-2 satellite was inserted into NASA's A-Train constellation in 2014 and flies about 6 minutes ahead of Aqua. OCO-2 provides the column-averaged carbon dioxide (CO_2) dry-air mole fraction (XCO_2) through passive spectroscopy based on hyperspectral radiance observations in three narrow wavelength regions, the Oxygen A-Band (~0.76 micron), the weak CO_2 band (~1.60 micron), and the strong CO_2 band (~2.06 micron). As shown in the inset of Figure 2, it takes measurements in eight footprints across a narrow swath. Each of the footprints has a size around 1-2 km, and the spectra for the three bands are provided by separate, co-registered spectrometers (Crisp et al., 2015).

The OCO-2 data products of 1) Level 1B calibrated and geolocated science radiance spectra (L1bScND), 2) standard Level 2 geolocated XCO_2 retrievals results (L2StdND), 3) meteorological parameters interpolated from GMAO (L2MetND) at OCO-2 footprint location are downloaded from NASA GES DISC (Goddard Earth Science Data Archive and Information Services Center) data archive (https://oco2.gesdisc.eosdis.nasa.gov/data/OCO2_DATA). Since MODIS on Aqua overflies a scene 6 minutes after OCO-2, the clouds move with the wind over this time period. We therefore added a wind correction on top of the parallax-corrected cloud fields obtained from MODIS (section 2.2.1). This was done with the 10 m wind speed data from L2MetND (see Appendix D2). For the same scene as shown in Figure 2, Figure 3 shows (a) COT, (b) CER, and (c) CTH, all corrected for both parallax and wind effects (these corrections are shown in Figure A2 in Appendix D). The parallax and wind corrections are imperfect as certain assumptions are involved. For example, they rely on the cloud top height from the MODIS cloud product. In addition, they process the whole scene with one single sensor viewing geometry. To minimize artifacts introduced by the assumptions, one can apply the simulation to a smaller region.

Deleted: reflectance, we used

Deleted: for

Deleted: -

Deleted: are

Deleted: -

Deleted: B2

Deleted: effect

Deleted: A1

Deleted: B

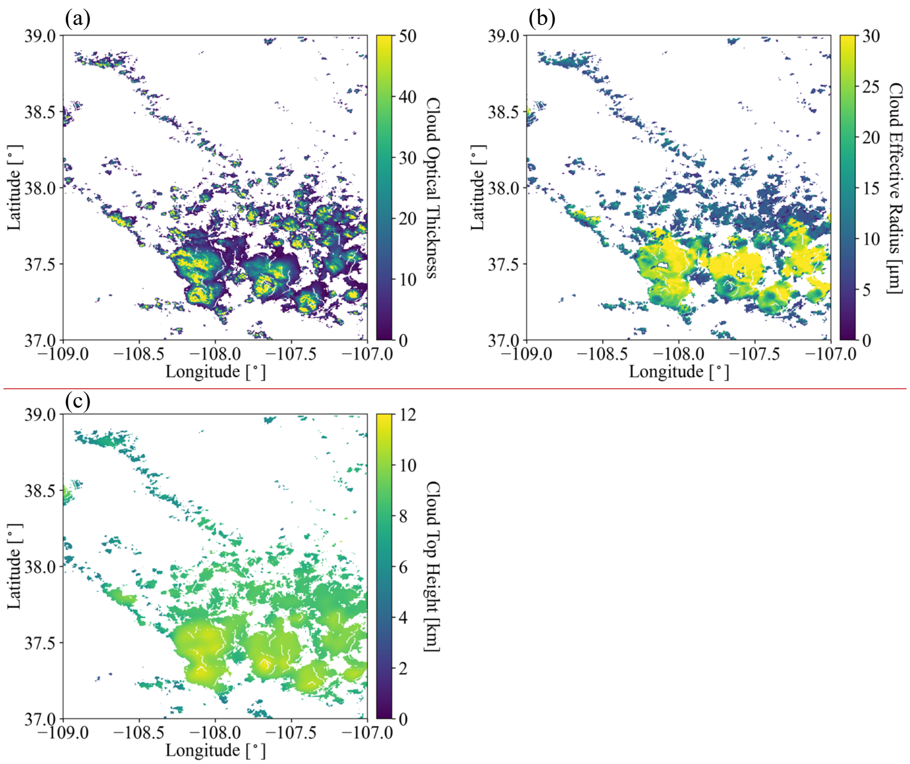

Figure 3. **(a)** Cloud optical thickness derived from MODIS L1B radiance at 650 nm by the two-stream approximation (Eq. A2), **(b)** cloud effective radius (units: μm), and **(c)** cloud top height (units: km) collocated from the MODIS L2 cloud product. The locations of the cloudy pixels were shifted to account for parallax and wind effects. The parallax correction ranged from near 0 for low clouds and 1 km for high clouds (10 km CTH). The wind correction was around 0.8 km, given the average wind speed of 2 m/s to the east.

The OCO-2 data (L2StdND) themselves only provide sparse surface reflectance for the footprints that are clear, while EaR^{3}T requires surface albedo for the whole domain. Therefore, we used MYD09A1 as a starting point. However, since MODIS does not have a channel in the Oxygen A-Band, MODIS band 2 (860 nm) was used as a proxy for the 760 nm OCO-2 channel as follows: we collocated the OCO-2 retrieved 760 nm surface reflectance R_{OCO} within the corresponding 860 nm MODIS MYD09A1 data R_{MOD} as shown in Figure 4a (same domain as Figures 2 and 3) and calculated a scaling factor assuming a linear relationship between R_{OCO} and R_{MOD} ($R_{OCO} = a \cdot R_{MOD}$). Figure 4b shows R_{OCO} versus R_{MOD} for all cloud-free OCO-2 footprints. The red line shows a linear regression (derived scale factor $a=0.93$). Optionally, the OCO-2-scaled MODIS-derived surface reflectance fields can be replaced by the OCO-2 surface reflectance products for pixels where they are available. The scaled surface reflectance is then treated as surface albedo input to the RTM assuming a Lambertian surface.

Deleted: Scaling is also applied for the weak and strong CO_2 channels, even though there are matching MODIS channels.

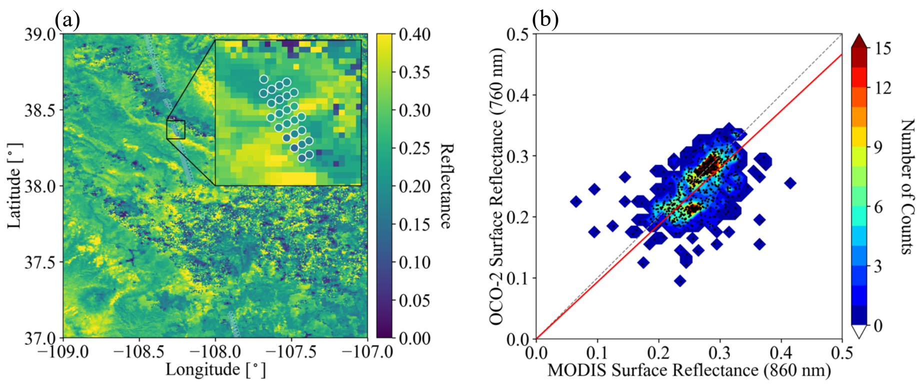

Figure 4. **(a)** Surface reflectance from the OCO-2 L2 product in the Oxygen A-band (near 760 nm), overlaid on the surface reflectance from the MODIS MYD09 product at 860 nm. **(b)** OCO-2 surface reflectance at 760 nm versus MODIS surface reflectance at 860 nm, along with linear regression ($y=ax$) as indicated by the red line (slope $a=0.9337$).

2.2.3 Advanced Himawari Imager (AHI)

The Advanced Himawari Imager (AHI, used for App. 3) is a payload on Himawari-8, a geostationary satellite operated by the Meteorological Satellite Center (MSC) of the Japanese Meteorological Agency. The AHI provides 16 channels of spectral radiance measurements from the shortwave (0.47µm) to the infrared (13.3µm). During CAMP^{2}Ex, the NASA in-field operational team closely collaborated with the team from MSC to provide AHI satellite imagery at the highest resolution over the Philippine Sea. From the AHI imagery, the cloud product generation system - Clouds from AVHRR Extended System (CLAVR-x), was used to generate cloud products from the AHI imagery (Heidinger et al., 2014). The cloud products from CLAVR-x include cloud optical thickness, cloud effective radius, and cloud top height at 2 (at nadir) to 5

Deleted: APP

km spatial resolution. Since AHI provides continuous regional scans every 10 minutes the AHI cloud product has a temporal resolution of 10 minutes.

2.2.4 Spectral Sunshine Pyranometer (SPN-S)

The SPN-S is a prototype spectral version of the commercially available global-diffuse SPN1 pyranometer (Wood et al., 2017; Norgren et al., 2022). The radiometer uses a 7-detector design in combination with a fixed shadow mask that enables the simultaneous measurement of both diffuse and global irradiances, from which the direct component of the global irradiance is calculated via subtraction. The detector measures spectral irradiance from 350 to 1000 nm, and the spectrum is sampled at 1 nm resolution with 1 Hz timing.

During the CAMP^{2}Ex mission, the SPN-S was mounted to the top of the NASA P-3 aircraft where it sampled downwelling solar irradiance. To ensure accurate measurements, pre- and post-mission laboratory-based calibrations were completed using tungsten "FEL" lamps that are traceable to a National Institute of Standards and Technology standard. Additionally, the direct and global irradiances were corrected for deviations of the SPN-S sensor plane from horizontal that are the result of changes in the aircraft's pitch or roll. This attitude correction applied to the irradiance data is a modified version of the method outlined in Long et al. (2010). However, whereas Long et al. (2010) employ a "box" flight pattern to characterize the sensor offset angles, in this study an aggregation of flight data containing aircraft heading changes under clear-sky conditions are used as a substitute. The estimated uncertainty of the SPN-S system is 6 to 8%, with 4 to 6% uncertainty stemming from the radiometric lamp calibration process, and up to another 2% resulting from insufficient knowledge of the sensor cosine response. The stability of the system under operating conditions is 0.5%. A thorough description of the SPN-S and its calibration and correction procedures is provided in Norgren et al. (2022). In this paper (App. 3) only the global downwelling irradiance sampled by the 745 nm channel is used.

Deleted: is

Deleted: APP

2.2.5 Airborne All-Sky Camera (ASC)

The All-Sky Camera (used for App. 4) is a commercially available camera (ALCOR ALPHEA 6.0CW[5]) with fish-eye optics for hemispheric imaging. It has a Charge-Coupled Device

Deleted: APP

[5]https://www.alcor-system.com/common/allSky/docs/ALPHEA_Camera%20ALL%20SKY%20CAMERA_Doc.pdf last accessed on April 24, 2022.

(CCD) detector that measures radiances in red, green, and blue channels. Radiometric and geometric calibrations were performed at the Laboratory of Atmospheric and Space Physics at the University of Colorado Boulder. The three-color channels are centered at 493, 555, and 626 nm for blue, green, and red, respectively, with bandwidths of 50 – 100 nm. Only radiance data from the red channel are used in this paper. The spatial resolution of the ASC depends on the altitude of the aircraft and the viewing zenith angle. Across the hemispheric field of view of the camera, the resolution of the field angle is approximately constant, at about 0.09º. At a flight level of 5 km, this translates to a spatial resolution of 8 m at nadir. However, due to accuracy limitations of the geometric calibration and the navigational data from Inertial Navigation System (INS), the nadir geolocation accuracy could only be verified to within ±50 m. During the CAMP^{2}Ex flights, the camera exposure time was set manually to minimize saturation of the detector. The standard image frame rate is 1 Hz. The precision of the camera radiances is on the order of 1%, and the radiometric accuracy is 6 – 7%.

Deleted: were

3. EaR^{3}T Procedures

In the previous section, we described the general workflow of EaR^{3}T applications, along with relevant data. In this section, we will focus on the specific implementation of the workflow through the EaR^{3}T software package. It is a toolbox for 3D-RT with modules for automatic input data download and processing, generation of radiative and optical properties of surface, atmospheric gases, clouds and aerosols, wrappers for 3D-RT solvers and output post-processing, with the end goal to simulate radiances and irradiances along entire satellite orbits or aircraft flight tracks. Unlike established radiative transfer packages such as libRadtran (Mayer and Kylling, 2005; Emde et al., 2016), which provide extensive libraries of optical properties along with a selection of solvers, EaR^{3}T focuses on automated radiative transfer for two- or three-dimensional cloud, aerosol, and surface input data, and therefore only comes with minimal options for optical properties, and solvers. The initial release (version 0.1.0) is available at https://github.com/hong-chen/er3t.

We will now walk through the OCO-2 and MODIS simulator applications with the codes `examples/01_oco2_rad-sim.py` (App. 1) and `examples/02_modis_rad-sim.py` (App. 2). The data acquisition (first step in Figure 1) uses functions in `er3t/util`. App. 1 and

Deleted: APP

Deleted: APP

Deleted: APP

App. 2 use the functions in `er3t/util/modis.py` and `er3t/util/oco2.py` for downloading the MODIS and OCO-2 data files from the respective NASA data archives and for processing the data (e.g., geo-mapping, gridding etc.). The user supplies minimum input (date and time, as well as latitudes and longitudes of the region of interest), which need to be specified in `download_modis_https` and `download_oco2_https` (from `er3t/util`). For example, for App. 1 and App. 2, the only user inputs are the date and time and the region of interest – in this case September 2, 2019, with the westernmost, easternmost, southernmost, and northernmost longitudes and latitudes of 109°W, 107°W, 37°N, and 39°N. In order for EaR^{3}T to access any data archives such as NASA Earthdata, the user needs to create an account with them and store the credentials locally (detailed instructions are provided separately along with the EaR^{3}T distribution).

After the data acquisition step, the satellite data are fed into the pre-processing step for 1) atmospheric gases (`er3t/pre/atm`), 2) clouds (`er3t/pre/cld`), 3) surface (`er3t/pre/sfc`) as shown in Figure 1. In the default configuration of the App. 1, the standard US atmosphere (Anderson et al., 1986; included in the EaR^{3}T repository) is used within `atm`. EaR^{3}T supports the input of user-specified atmospheric profiles, e.g., atmospheric profiles from reanalysis data for App. 2 as described in Schmidt et al. (2022), by making changes in `atm_atmmod` (from `er3t/pre/atm`). Subsequently, molecular scattering coefficients are calculated by `cal_mol_ext` (from `er3t/util`), and absorption coefficients for atmospheric gases are generated by (`er3t/pre/abs`). At the current development stage, two options are available:

1. Line-by-line (used by App. 1): The repository includes a sample file of absorption coefficient profiles for a subset of wavelengths within OCO-2's Oxygen A-Band channel, corresponding to a range of atmospheric transmittance values from low (opaque) to high (so-called "continuum" wavelength). They were generated by an external code (Schmidt et al., 2022) based on OCO-2's line-by-line absorption coefficient database (ABSCO, Payne et al., 2020). For each OCO-2 spectrometer wavelength within a given channel, hundreds of individual absorption coefficient profiles at the native resolution of ABSCO need to be considered across the instrument line shape (ILS, also known as the slit function) of the spectrometer. The ILS, as well as the incident solar irradiance, are also included in the file. In subsequent steps, EaR^{3}T performs RT calculations at the native spectral resolution of

Deleted: APP
Deleted: oco
Deleted: APP
Deleted: APP
Deleted: APP
Deleted: APP
Deleted: APP
Deleted: there are
Deleted: , spectrally spaced
Deleted: , and ranging
Deleted: OCO-2 Oxygen A-Band

ABSCO, but then combines the output by convolving with the ILS and outputs OCO-2 radiances or reflectances at the subset of wavelengths. For probabilistic (Monte Carlo) RT solvers such as MCARaTS, the number of photons can be kept relatively low (e.g., 10^6 photons), and can be adjusted according to the values of the ILS at a particular ABSCO wavelength. Any uncertainty at the ABSCO spectral resolution due to photon noise is greatly reduced by convolving with the ILS for the final output.

2. Correlated-k (used by App. 2): This approach (Mlawer et al., 1997) is appropriate for instruments such as MODIS with much coarser spectral resolution than OCO-2, as well as for broadband calculations. In contrast to the line-by-line approach, RT calculations are not performed at the native resolution of the absorption database, but at Gaussian quadrature points (called "g's") that represent the full range of sorted absorption coefficients, and then combined using Gaussian quadrature weights. The repository includes an absorption database from Coddington et al. (2008), developed specifically for a radiometer with moderate spectral resolution on the basis of HITRAN (high-resolution transmission molecular absorption database) 2004 (Rothman et al., 2005). It was created for the ILS of the airborne Solar Spectral Flux Radiometer (SSFR, Pilewskie et al., 2003), but is applied to MODIS here, which has a moderate spectral resolution of 8-12 nm with 20-50 nm bandwidths. It uses 16 absorption coefficient bins (g's) per target wavelength (this could either be an individual SSFR or a MODIS channel), which are calculated by EaR^{3}T with the Coddington et al. (2008) database using the mixing ratios of atmospheric gases in the previously ingested profile. In future implementations, the code will be updated to enable flexible ILS and broadband calculations.

The `er3t/pre/cld` module calculates extinction, thermodynamic phase, and effective droplet radius of clouds from the input data. The `er3t/pre/pha` module creates the required single scattering albedo and scattering phase function. The default is a Henyey-Greenstein phase function with a fixed asymmetry parameter of 0.85. Along with the current distribution (v0.1.0) of EaR^{3}T, the Mie phase functions based on thermodynamic phase, effective droplet radius, and wavelength are supported. In this study, App. 1 and App. 2 use Mie phase functions calculated from Legendre polynomial coefficients (originally distributed along with libRadtran) based on the wavelength and cloud droplet effective radius. In the future, EaR^{3}T will include stand-alone phase functions, which can be chosen on the basis of droplet size distributions in addition to effective

Deleted: APP

Deleted: It is, however, recommended to also install libRadtran to…

Deleted: enable the usage of

Formatted: Superscript

Deleted: APP

Deleted: APP

radius. It is also possible to include aerosols in a similar fashion as clouds. This is done with the `er3t/pre/aer` module. In the case of aerosols, spectral single scattering albedo and asymmetry parameter are required as inputs in addition to the extinction fields.

After the optical properties are calculated, they are passed into the 3D-RT step (`er3t/rtm/mca`). In addition to MCARaTS, planned solvers for the future include MYSTIC (Monte Carlo code for the physically correct tracing of photons in cloudy atmospheres, Mayer, 2009) and SHDOM (Spherical Harmonic Discrete Ordinate Method, Evans, 1998; Pincus and Evans, 2009). This step performs the setup of RT solver-specified input parameters and data files, distributing runs over multiple Central Processing Units (CPUs), and post-processing RT output files into a single, user-friendly HDF5 file. For example, when radiance is specified as output (default in App. 1 and App. 2), key information such as the radiance field and its standard deviation are stored in the final HDF5 file (details see Table 1).

While the EaR^{3}T repository comes with various applications such as App. 1 and App. 2, described above, the functions used by these master or 'wrapper' programs can be organized in different ways, where the existing applications serve as templates for a quick start when developing new applications. The functions used by the master code pass information through the various steps as Python objects. For example, in `examples/01_oco2_rad-sim.py`, the downloaded and processed satellite data are stored into the `sat` object. Later, the `sat` object is passed into an EaR^{3}T function to create the `cld` object that contains cloud optical properties. Similarly, EaR^{3}T provides functions to create the `atm`, and `sfc` objects with optical properties for atmospheric gases and the surface. These objects (`atm`, `cld`, `sfc`) are in turn passed on to solver-specific modules for performing RT calculations. The user can choose to save the data of the intermediate objects into Python pickle files after the first run. In this way, multiple calls with identical input can re-use existing data, which accelerates the processing time of EaR^{3}T. Unless the user specifies the `overwrite` keyword argument in the object call to reject saving pickle files, these shortcuts save significant time. Moreover, EaR^{3}T is capable of distributing simulations over multiple CPUs to accelerate the calculations, which is useful for potential future application of later EaR^{3}T or EaR^{3}T-like codes in operational or large-scale data processing.

In the following sections, we discuss results obtained from EaR^{3}T, starting with those from `examples/01_oco2_rad-sim.py` and `examples/02_modis_rad-sim.py` (section 4), `examples/03_spns_flux-sim.py` (section 5), and concluding with

Deleted: APP

Deleted: APP

Deleted: The EaR^{3}T documentation only provides detailed instructions of installing the RT solvers (currently only MCARaTS) and libRadtran.

Deleted: APP

Deleted: APP

`examples/04_cam_nadir_rad-sim.py` (section 6). The detailed RT setup for the applications is provided Table A1 in Appendix A.

4. EaR^{3}T as a 3D Satellite Radiance Simulator

This section demonstrates the automated 3D radiance simulation for satellite instruments by EaR^{3}T for OCO-2 and MODIS measured radiance based on publicly available MODIS retrieval products. The OCO-2 application is an example of radiance consistency between two distinct satellite instruments where the measurements of one (here, OCO-2) are compared with the simulations based on data products from the other (here, MODIS). The MODIS application, on the other hand, is an example of radiance self-consistency. We will show how inconsistencies can be used for detecting cloud and surface property retrieval biases.

4.1 OCO-2 (App. 1)

The OCO-2 radiance measurements at 768.52 nm for our sample scene in the context of MODIS imagery were shown in Figure 2. For that track segment, Figure 5a shows the simulated radiance along with the measurements as a function of latitude. The radiance was averaged over every 0.01° latitude window from 37° N to 39° N (the standard deviation within the bin indicated by the shaded color). In clear-sky regions (e.g., around 38.2º N), the simulations (red) are systematically higher than the measurements (black), even though the footprint-level OCO-2 retrieval was used to scale the MYD09 surface reflectance field as described in section 2.2.2 (Figure 4). This is because, unlike the MYD09 algorithm which relies on multiple overpasses and multiple-days for cloud-clearing, the OCO-2 retrieval is done for any clear footprint. Clouds in the vicinity lead to enhanced diffuse illumination that is erroneously attributed to the surface reflectance itself. The EaR^{3}T IPA calculations of the clear-sky pixels (blue) essentially reverse the 3D effect and therefore match the observations better. The 3D calculations enhance the reflectance through the very same 3D cloud effects that led to the enhanced surface illumination in the first place. It is possible to correct this effect by down-scaling the surface reflectance according to the ratio between clear-sky 3D and IPA calculations, but this process is currently not automated.

Deleted: four

Deleted: in Table 2

Deleted: ¶
¶ ... [1]

Deleted: APP

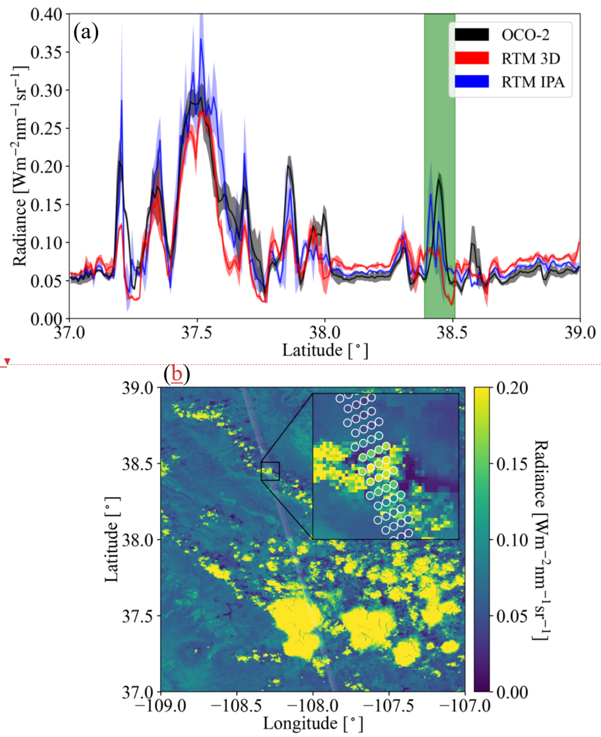

Figure 5. (a) Latitudinally averaged (0.01° spacing) radiance calculations from EaR^{3}T (red: 3D, blue: IPA) and OCO-2 measured radiance at 768.52 nm (black) The green shaded area indicates the inset shown in (b). **(b)** The same as Figure 2 except OCO-2 measured radiance overlaid on IPA radiance simulations at 768.52 nm. The solar zenith angle (SZA) for the radiance simulation case is 33.57°.

Deleted:

In the cloudy locations, the IPA calculations match the OCO-2 observations on a footprint-by-footprint level (see Figure 5b), demonstrating that wind and parallax corrections were performed successfully. Of course, there is not always a perfect agreement because of morphological changes in the cloud field over the course of six minutes. It is, however, apparent that the 3D calculations agree to a much lesser extent with the observations than the IPA calculations. Just like the mismatch for the clear-sky pixels indicates a bias in the input surface reflectance, the bias here means that the input cloud properties (most importantly COT) are inaccurate. For most of the reflectance peaks, the 3D simulations are too low, which means that the input COT is biased low. This is due to 3D cloud effects on the MODIS-based cloud retrieval. Since they are done with IPA, any net horizontal photon transport is not considered, which leads to an apparent surface brightening as noted above, at the expense of the cloud brightness. As a result, the COT from darker clouds is significantly underestimated. This commonly known problem (Barker and Liu, 1995), with several aspects discussed in the subsequent EaR^3T applications, can be identified by radiance consistency checks such as the one shown in Figure 5, and mitigated by novel types of cloud retrievals that do take horizontal photon transport into account (section 6).

4.2 MODIS (App. 2)

Deleted: APP

To go beyond the OCO-2 track and understand the bias between simulated and observed radiances from a domain perspective, we now consider the radiance simulations for the MODIS 650 nm channel. The setup is exactly the same as for the OCO-2 simulations, except that 1) the viewing zenith angle is set to the average viewing zenith angle of MODIS within the shown domain (instead of OCO-2), and 2) the surface reflectances from MYD09 are used directly, this time from the 650 nm channel without rescaling. Figure 6a shows the MODIS measured radiance field, while Figure 6b shows the EaR^3T 3D simulations. Visually, the clouds from the EaR^3T simulation are generally darker than the observed clouds, which is in line with our aforementioned explanation of net horizontal photon transport. They are also blurrier because radiative smoothing (Marshak et al., 1995) propagates into the retrieved COT fields, which are subsequently used as input to EaR^3T. To look at darkening and smoothing effects more quantitatively, Figure 7 shows a heatmap plot of simulated radiance versus observed radiance. It shows that the radiance for cloud-covered pixels (labeled "cloudy") from EaR^3T are mostly low-biased while good agreement between simulations and observations was achieved for clear-sky radiance (labeled "clear-sky"). The good agreement over clear-sky regions is expected. As mentioned above, we use MYD09 as surface reflectance input, which in contrast to the OCO-2 surface reflectance product is appropriately cloud-screened and therefore does not have a reflectance high bias. There is, of course, a reflectance enhancement in the vicinity of clouds, but that is captured by the EaR^3T calculations. The fact that the calculations agree with the observations even for clear-sky pixels in the vicinity of clouds, shows that the concept of radiance consistency works to ensure correct satellite retrievals even in the presence of clouds. It also corroborates our observation from section 4.1 that COT_{IPA} is low biased.

Since the MODIS reflectance is *not* self-consistent with respect to COT_{IPA} as shown for the *cloudy* pixels in Figure 7, we can identify a bias in the cloud properties even without knowing the ground truth of COT. On the other hand, successful closure in radiance (self-consistency) would provide an indication that the input fields including COT are accurate, although it is certainly a weaker metric than direct verification of the retrievals through aircraft satellite retrieval validation with in-situ instruments.

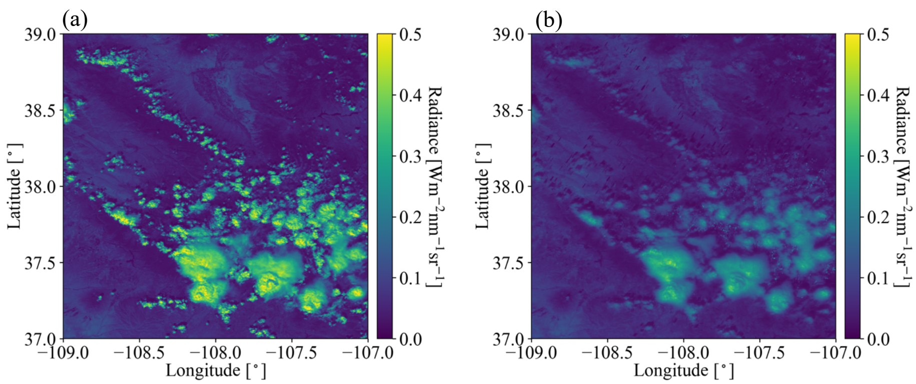

Figure 6. **(a)** MODIS measured radiance in channel 1 (650 nm). **(b)** Simulated 3D radiance at 650 nm from EaR^3T. The solar zenith angle for the radiance simulation case is 34.42°.

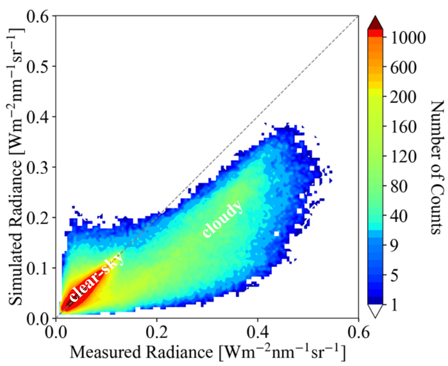

Figure 7. Heatmap plot of EaR^3T simulated 3D radiance vs. MODIS measured radiance at 650 nm.

Summarizing the two satellite radiance simulator applications, one can say that EaR^{3}T enables a radiance consistency check for inhomogeneous cloud scenes. We demonstrated that a lack of simulation-observation consistency (MODIS versus OCO-2) and self-consistency (MODIS versus MODIS) can be traced back to biased surface reflectance or cloud fields in the simulator input. This can become a diagnostic tool for the quality of retrieval products from future or current missions, even when the ground truth is not known. It should be pointed out that the vertical extent of the clouds affects the simulated radiance – the larger the vertical extent, the larger the 3D effects (more horizontal photon transport). Since we make the assumption of a cloud geometric thickness of 1 km if no thickness information is provided, the simulated radiance at the satellite sensor level is valid for that proxy cloud only. For deeper clouds, the simulated radiance would be even lower. Either way, the comparison with the actual radiance measurements will reveal a lack of closure. Additionally, although the clouds introduce the lion's share of the 3D bias that is identified by the radiance consistency check, additional discrepancies can be introduced in different ways. For example, the topography (mountainous region in Colorado) is not considered by MCARaTS (it is considered by MYSTIC, but this solver has not been implemented yet).

For technical reference: The MODIS simulation (domain size of [Nx=1188, Ny=1188]) took about one hour on a Linux workstation with 12 CPUs for three 3D RT runs with 10^8 photons each. With a slightly modified setup and parallelization, the automation can be easily applied for entire satellite orbits, although more research is required to optimize the computation speed depending on the desired output accuracy.

5. EaR^{3}T as 3D Aircraft Irradiance Simulator (App. 3)

Deleted: APP

In contrast to the previous applications that focused on satellite remote sensing, we will now be applying EaR^{3}T to quantify 3D cloud retrieval biases through direct, systematic validation of imagery-derived *irradiances* against aircraft measurements, instead of using the indirect path of radiance consistency in section 4. Previous studies (e.g., Schmidt et al., 2007; Kindel et al., 2010) conducted radiative closure between remote sensing derived and measured irradiance using isolated flight legs as case studies. Here, with the efficiency afforded by the automated nature of EaR^{3}T, we are able to conduct radiative closure of irradiance through a statistical approach that employs campaign-scale amounts of measurement data. Specifically, we used EaR^{3}T to perform large-scale downwelling irradiance simulations at 745 nm based on geostationary cloud retrievals from AHI for the CAMP^{2}Ex campaign, and directly compare these simulations to the SPN-S measured irradiances onboard the P-3 aircraft. This is done for all below-cloud legs from the entire campaign with the aim to assess the degree to which satellite-derived near-surface irradiances reproduce the true conditions below clouds.

The irradiance simulation process is similar to the previously described radiance simulation in section 4, with only a few modifications. First, we used cloud optical properties from the AHI cloud product (COT, CER and CTH) as direct inputs into EaR^{3}T. Secondly, we used a constant ocean surface reflectance value of 0.03. Such simplification in surface albedo is made under the assumption that 1) the ocean surface is calm with no whitecaps, and that 2) the Lambertian bidirectional reflectance distribution function (BRDF) is sufficient (instead of directionally dependent BRDF) to represent surface albedo for the irradiance calculation. Since the ocean surface albedo can greatly differ from 0.03 when the Sun is extremely low (Li et al., 2006), we excluded data under low-Sun conditions where the SZA is greater than 45°. Lastly, since EaR^{3}T can only perform 3D simulations for a domain at a single specified solar geometry, we divided each CAMP^{2}Ex research flight into small flight track segments where each segment contains 6 minutes of flight time. The size and shape of the flight track segments can vary significantly due to the aircraft maneuvers, aircraft direction, aircraft speed, etc. For each flight track segment, EaR^{3}T performs irradiance simulations for a domain that extends half a degree at an averaged solar zenith angle. In contrast to the radiance simulation output, which is two-dimensional at a specified altitude and sensor geometry, the irradiance simulation output is three dimensional. In addition to x (longitude) and y (latitude) vectors, it has a vertical dimension along z (altitude). From the simulated three-dimensional irradiance field, the irradiance for the flight track segment is linearly interpolated to the x-y-z location (longitude, latitude, and altitude) of the aircraft. EaR^{3}T automatically sub-divides the flight track into tiles encompassing track segments, and extracts the necessary information from the aircraft navigational data. Based on the aircraft time and position, EaR^{3}T downloads the AHI cloud product that is closest in time and space to the domain containing the flight track segment.

Figure 8 shows the simulated irradiance for a sample flight track below clouds on 20 September, 2019. Figure 8a shows the flight track overlaid on AHI imagery. Figure 8b shows 3D (in red) and IPA (in blue) downwelling irradiance simulations for the highlighted flight track in Figure 8a, as well as measurements by the SPN-S (in black). Since the 3D and IPA simulations are performed separately at discrete solar and sensor geometries for each flight track segment based on potentially changing cloud fields from one geostationary satellite image to the next, discontinuities in the calculations (indicated by gray dashed lines) are expected. The diffuse irradiance (downwelling and upwelling) can also be simulated and compared with radiometer measurements (not shown here). Since the irradiance was simulated/measured below clouds, high values of downwelling irradiance indicate thin-cloud or cloud-free regions while low values of downwelling irradiance indicate thick-cloud regions. The simulations successfully captured this general behavior – clouds thickened from west to east until around 121.25° E, and thinned eastwards. However, the fine-scale variabilities in irradiance were not captured by the simulations due to the coarse resolution of COT in the AHI cloud product (3-5 km). Additionally, the simulations also missed the clear-sky regions in the very east and west of the flight track as indicated by high downwelling irradiance values measured by SPN-S. This is probably also due to the coarse resolution of the AHI COT product where small cloud gaps are not represented. Large discrepancies between simulations and observations occur in the mid-section of the flight track where clouds are present (e.g., longitude range from 121.15° to 121.3°). Although the 3D calculations differ somewhat from the IPA results, they are both biased high, likely because the input COT (the IPA-retrieved AHI product) is biased low. This bias is caused by the same mechanism that was discussed earlier in the MODIS examples (section 4.2). This begs the question whether this is true for the entire field mission. To answer the question, we performed a *systematic* comparison of the cloud transmittance for *all* available below-cloud flight tracks from CAMP^{2}Ex, using EaR^{3}T's automated processing pipeline. The output of this pipeline is visualized in time-synchronized flight videos (Chen et al., 2022), which show the simulations and observations along all flight legs point by point. These videos give a glimpse of the general cloud environment during the field campaign from the geostationary satellite perspective.

Deleted: from MODIS

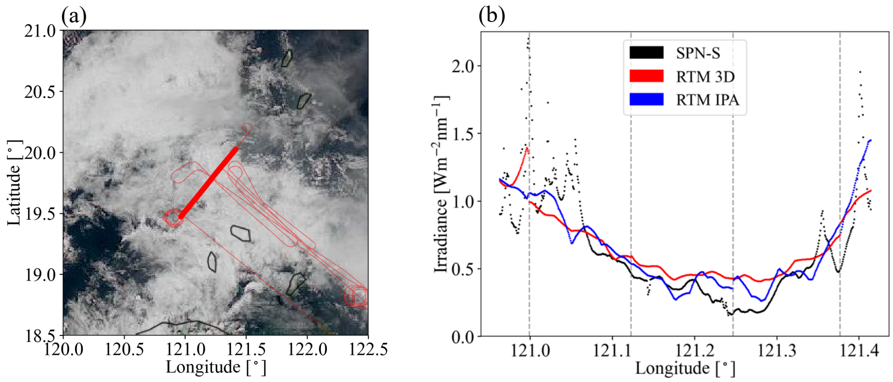

Figure 8. **(a)** Flight track overlay HIMAWARI AHI RGB imagery over the Philippine Sea on 20 September, 2019. The thin line shows the entire flight track within the domain. The thick line highlights the specific leg analyzed in (b). **(b)** Measured downwelling irradiance from SPN-S at 745 nm and calculated 3D and IPA irradiance from EaR^{3}T for the highlighted flight track in (a).

For this comparison, we use transmittance instead of irradiance. The transmittance is calculated by dividing the downwelling irradiance below clouds ($F_{\downarrow}^{bottom}$) by the downwelling irradiance at the top of the atmosphere extracted from the Kurucz solar spectra ($F_{\downarrow}^{TOA}$; Kurucz, 1992) at incident solar zenith angle (SZA), where $Transmittance = F_{\downarrow}^{bottom} \big/ (F_{\downarrow}^{TOA} \cdot \cos(SZA))$. Thus the transmittance has less diurnal dependence than the irradiance. Figure 9 shows the histograms of the simulated and measured cloud transmittance from all below-cloud legs. The average values are indicated by dashed lines. Although the averaged values of IPA and 3D transmittance are close, their distributions are different. Only the 3D calculations and the measured transmittance reach values beyond 1. This occurs in clear-sky regions in the vicinity of clouds that receive photons scattered by the clouds as previously discussed for the OCO-2 application.

Deleted: because it has less diurnal dependence

Deleted: completely

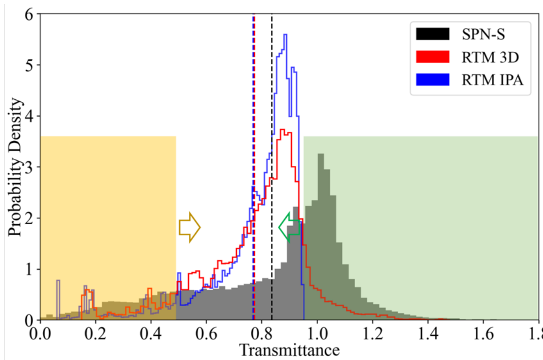

Figure 9. Histogram of measured transmittance from SPN-S at 745 nm (black) and calculated 3D (red) and IPA (blue) transmittance from EaR^{3}T for all the below-cloud flight tracks during CAMP^{2}Ex in 2019. The mean values are indicated by dashed lines. The yellow (green) shaded area represents the relatively low (high) transmittance region where the probability density of the observed transmittance (black) is greater than the calculations.

Deleted: Vice versa for the green shaded area.

Both the distribution and the mean value of the simulations are different from the observations – the simulation histograms peak at around 0.9 while the observation histogram peaks at around 1. The histograms indicate that the RT simulations miss most of the clear-sky conditions because of the coarse resolution of the AHI cloud product. If clouds underfill a pixel, AHI interprets the pixel as cloudy in most cases. This leads to an underestimation of clear-sky regions since cumulus and high cirrus were ubiquitous during CAMP^{2}Ex. The area on the left (highlighted in yellow) has low cloud transmittance associated with thick clouds. In this range, the histograms of the calculations are generally below the observations, and the PDF of the calculations is offset to the right (indicated by the yellow arrow). This means that the transmittance is overestimated by both IPA and 3D RT, and thus that the COT of thick clouds is underestimated, consistent with what we found before (Figure 8b). The high-transmittance end (highlighted in green) is associated with clear-sky and thin clouds. Here, the peak of the PDF is shifted to the left (green arrow), and the calculations are biased low. This is caused by a combination of 1) the overestimation in COT of thin clouds due a 3D bias in the AHI IPA retrieval, 2) the aforementioned resolution effect that underestimates the occurrence of clear-sky regions (or overestimation in cloud fraction), and 3) net horizontal photon transport from clouds into clear-sky pixels. Overall, the calculations underestimate the true transmittance by 10%. This might seem to contradict Figure 7, where the

Deleted: histogram

Deleted: s

Deleted: Overall, the low bias dominates, as is apparent from mean values of the distributions. There is an overall low bias of 10%, and the combined imager resolution and 3D effects do not compensate each other.

calculated reflected radiance was biased low due to the *underestimation* of COT in the heritage retrievals, which would correspond to an *overestimation* of the radiation transmitted by clouds. This effect is indeed apparent in the yellow-shaded area of Figure 9 (high COTs), but the means (dashed lines) show exactly the opposite. To understand that, one has to consider that the histogram depicts all-sky conditions, which include both cloudy and clear pixels. In this case, the direction of the overall (all-sky) bias follows the direction of the thin-cloud/clear bias, rather than the direction of the thick cloud bias. For different study regions of the globe with different cloud fractions, cloud size distributions, and possibly different imager resolutions, the direction and magnitude of the bias might be very different.

Summarizing, this application demonstrates that the EaR^{3}T's automation feature allows systematic simulation-to-observation comparisons. If aircraft observations are available, then closure between satellite-derived irradiance and suborbital measurements is a more powerful verification of satellite cloud retrieval products than the radiance consistency from the earlier stand-alone satellite applications. Even more powerful is the new approach to process the data from an entire field mission for assessing the quality of cloud products in a region of interest (in this case, the CAMP^{2}Ex area of operation).

6. EaR^{3}T for Mitigating 3D Cloud Retrieval Biases (App. 4)

In this section, we will use high-resolution imagery from a radiometrically calibrated all-sky camera flown during the CAMP^{2}Ex to isolate the 3D bias (sometimes referred to as IPA bias) and explore its mitigation with a newly developed CNN cloud retrieval framework (Nataraja et al., 2022). The CNN, unlike IPA, takes pixel-to-pixel net horizontal photon transport into account. It exploits the spatial context of pixels in cloud radiance imagery, and extracts a higher-dimensional, multi-scale representation of the radiance to retrieve COT fields as the output. It does so by learning on "training data", which in this case was input radiance and COT pairs synthetically generated by EaR^{3}T using LES data from the Sulu Sea. The best CNN model, trained on different coarsened resolutions of the data pairs, is included within the EaR^{3}T repository. For App. 4, this CNN is applied to real imagery data for the first time, which in our case are near-nadir observations by the all-sky camera (section 2.2.5) that flew in CAMP^{2}Ex.

The CNN model was trained at a single (fixed) sun-sensor geometry (solar zenith angle, SZA=29.2°; solar azimuth angle, SAA=323.8°, viewing zenith angle, VZA=0º), at a spatial

Deleted: We found that the bias between observed and satellite-derived cloud transmittance is partially caused by the coarse imager resolution, and partially by 3D effects, although other retrieval artifacts could also play a role. Although important for future research, it is beyond the scope of this paper to disentangle these effects.

Deleted: APP

Deleted: a

Deleted: -

Deleted: APP

Formatted: Indent: First line: 0.5"

resolution of 100 m. We therefore chose a camera scene with a matching SZA (28.9°), and rotated the radiance imagery to match SAA=323.8°, and subsequently gridded the 8-12 m native resolution camera data to 100 m. Figure 10a shows the RGB imagery captured by the all-sky camera over the Philippine Sea at 02:10:06 UTC on 5 October 2019. The Sun is located at the southeast (as indicated by the yellow arrow) and can be easily identified from the sun glint. Note that this image has not yet been geolocated; it is depicted as acquired in the aircraft reference frame. Figure 10b shows the rotated scene of the red channel radiance for the region encircled in yellow in Figure 10a. The sun (as indicated by the yellow arrow) is now at SAA=323.8°. The selected study region is indicated by the red rectangle in Figure 10b (6.4x6.4 km^2), where the raw radiance of the camera is gridded at 100 m resolution to match the spatial resolution of the training dataset of the CNN.

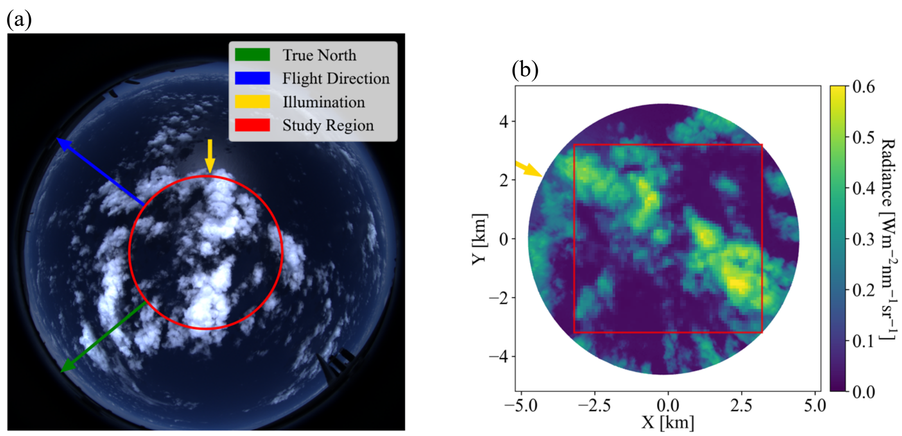

Figure 10. **(a)** RGB imagery of nadir-viewing all-sky camera deployed during CAMP^{2}Ex for a cloud scene centered at [123.392°E, 15.2744°N] over the Philippine Sea at 02:10:06 UTC on 5 October, 2019. The arrows indicate the true north (green), flight direction (blue), and illumination (where the sunlight comes from, yellow). **(b)** Red channel radiance measured by the camera for the circular area indicated by the red circle in (a). Red squared region shows gridded radiance with a pixel size of 64x64 and spatial resolution of 100 m.

From the radiance field, we used both the traditional IPA (based on the two-stream approximation) and the new CNN to retrieve COT fields. Figure 11 shows the COT_{IPA} and COT_{CNN}

Deleted: core area

Deleted: gridded radiance field is shown instead of the native-resolution imagery

Deleted: lines

Deleted: axis of the aircraft

Deleted: yellow

Deleted: and wing to wing

Deleted: across, black

Deleted: The yellow circle shows the approximate field of view that is geolocated for (b); the dots denote various directions from the nadir point. **(b)** Gridded radiance for the square area indicated by solid black lines in (a) with a pixel size of 64x64 and spatial resolution of 100 m

Deleted: Later for the comparison of COT and RT calculations, only the data from the red square box (50x50) is used. The solar position (azimuth) is indicated by the yellow arrow.

fields, which are visually quite different. For relatively thin clouds (e.g., at around {2, 1.8}), the CNN tends to retrieve larger COT values than COT_{IPA}. Also, it returns more spatial structure than the IPA (e.g., around {2,-1}). To assess how either retrieval performs, we now apply the radiance self-consistency approach introduced with MODIS data in section 4.2. Using both the IPA and the CNN retrieval as input, we had EaR^3T calculate the (synthetic) radiance that the camera should have observed if the retrieval were accurate. The clouds are assumed to be located at 1-2 km. Such an assumption is inferred from low-level aircraft observations of clouds on the same day. These radiance fields are shown in Figure 12a and 12b, and can be compared to Figure 12c. Seven edge pixels have been removed from the original domain because the CNN performs poorly at edge pixels, and because the 3D calculations use periodic boundary conditions.

Deleted: thick

Deleted: (x=2, y=22)

Deleted: the red box from Figure 10b

Deleted: ,

Deleted: which marks a region where

Deleted: 12

Deleted: 7

Deleted: . This was necessary

Deleted: ¶

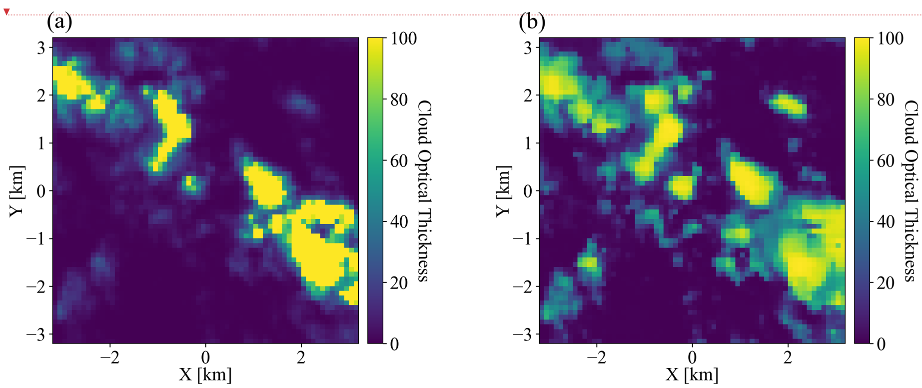

Figure 11. Cloud optical thickness for the gridded radiance in Figure 10b **(a)** estimated by IPA and **(b)** predicted by CNN.

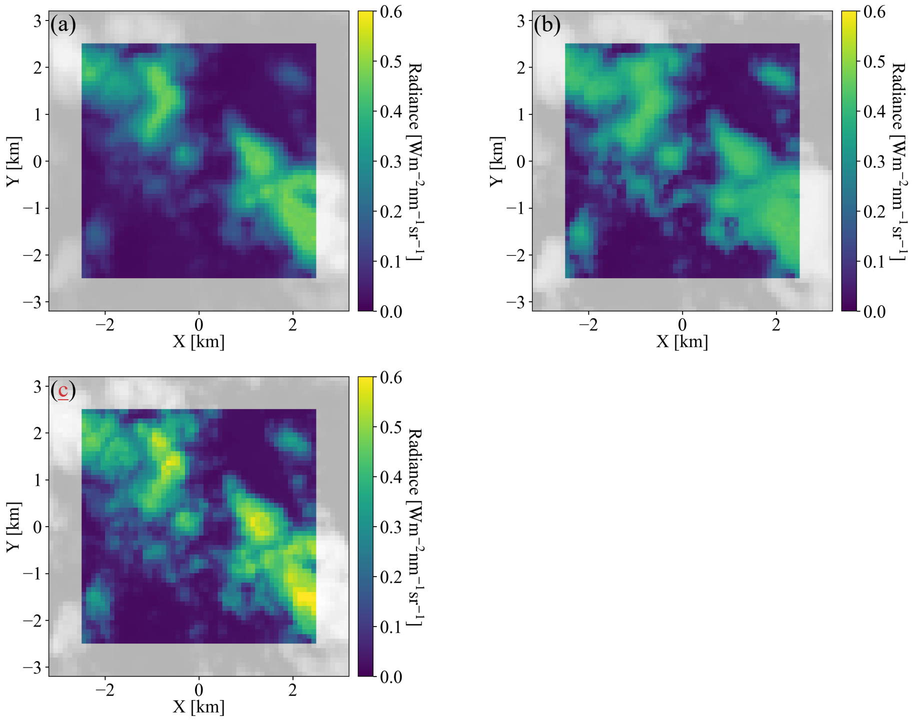

Figure 12. 3D radiance calculations from EaR^{3}T at 600 nm based on cloud optical thickness field **(a)** estimated by IPA, and **(b)** predicted by the CNN. The radiance measured by the all-sky camera (the same as Figure 10b) is provided in the same format at **(c)** for comparison. The calculations were originally performed for the 64x64 domain. Then 7 pixels along each side of the domain (contoured in gray) were excluded, which resulted in a 50x50 domain.

Deleted: Two-Stream approximation

Deleted: and

Formatted: Font: Bold

Deleted: ¶

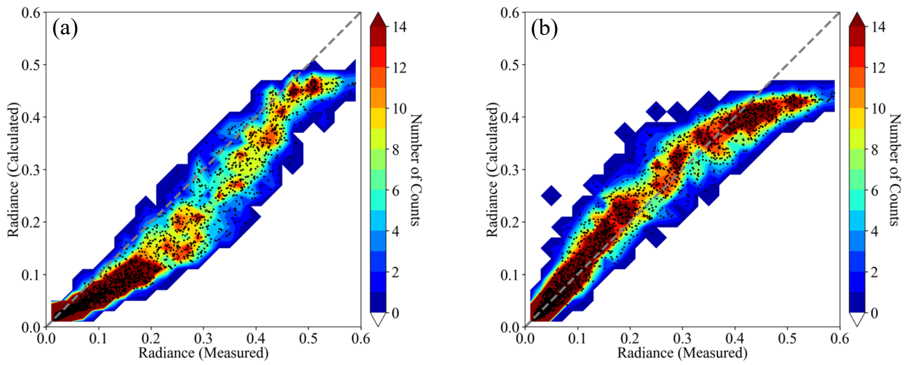

Figure 13. Scatter plot overlays 2D histogram of 3D radiance calculations at 600 nm based on cloud optical thickness **(a)** estimated by IPA and **(b)** predicted by the CNN vs. measured red channel radiance from all-sky camera.

Deleted: Two-Stream approximation

As evident from the brightest pixels in Figures 12b and 12c, the radiances simulated on the basis of the CNN COT input are markedly lower than actually observed by the camera. This is because the CNN was trained on a LES dataset with limited COT range that excluded the largest COT that occurred in practice. This means that the observational data went beyond the original training envelope of the CNN, which highlights the importance of choosing the CNN training data carefully for a given region. In Figure 13, the simulations are directly compared with the original observations, confirming that indeed the CNN-generated data are below the observations on the high radiance end. Otherwise, the CNN-generated radiances agree with the observations. In contrast, the IPA-generated data are systematically lower than the observations, over the dynamic range of the COT, which is indicative of the 3D retrieval bias that we discussed earlier. Here again, the self-consistency approach proves useful despite the absence of ground truth data for the COT. This is extremely helpful because in reality satellite remote sensing does not have the ground truth of COT, whereas radiance measurements are always available. For the CNN, the self-consistency of the radiance is remarkable for the thinner clouds (radiance smaller than 0.4), which encompass 83.5% of the total number of image pixels.

Deleted: 10b

Deleted: By

Finally, we use EaR^{3}T to propagate the 3D cloud retrieval bias into the associated bias in estimating the cloud radiative effect from passive imagery retrievals, which means that we are returning from a remote sensing to an energy perspective (irradiance) at the end of the paper. The calculated cloud radiative effects (CRE) of both below-clouds (at the surface) and above-clouds (at 3 km) are shown in Figure 14a and 14b. The most important histograms are those from 3D irradiance calculations based on the CNN retrievals (gray solid line), as this combination would be used in a next-generation framework for deriving CRE from passive remote sensing, and the other would be IPA irradiance calculations based on the IPA retrieval (red solid line), as done in the traditional (heritage) approach. The dashed lines are the other combinations. The mean values (red vs. gray) indicate that in our case the traditional approach would lead to a high bias of more than to 25% both at the surface and above clouds. Here again, 3D biases do not cancel each other out in the domain average. If the CNN had better fidelity even for optically thick clouds, the real bias in CRE would be even larger. A minor, but interesting finding is that regardless of which COT retrieval is used, the mean CRE is very similar for IPA and 3D irradiance calculations (e.g., $CRE_{IPA}(COT_{CNN}) \approx CRE_{3D}(COT_{CNN})$, blue dashed line overlay gray solid line), even though the PDFs are very dissimilar. By far the largest impact on accuracy comes from the retrieval technique, not from the subsequent CRE calculations. Here again, the self-consistency check turns out as a powerful metric to assess retrieval accuracy. Of course, we only used a single case in this part of the paper. For future evaluation of the CNN versus the IPA, one would need to process larger quantities of data in an automated fashion as done in the first part of the paper. This is beyond the scope of this introductory paper, and will be included in future releases of EaR^{3}T and the CNN.

Deleted: black

Deleted: black

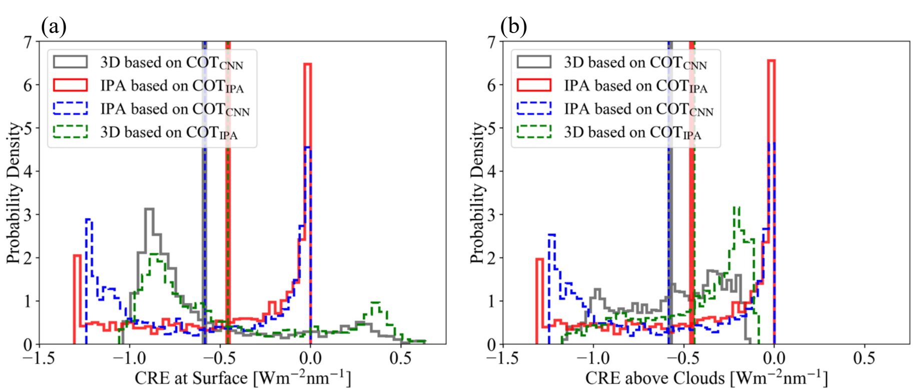

Figure 14. Histograms of cloud radiative effects derived from 1) 3D irradiance calculations based on COT_{CNN} (solid gray), 2) IPA irradiance calculations based on COT_{IPA} (solid red), 3) IPA irradiance calculations based on COT_{CNN} (dashed blue), and 4) 3D irradiance calculations based on COT_{IPA} (dashed green) both **(a)** at the surface and **(b)** above the clouds. The mean values are indicated by vertical lines.

Deleted: black

7. Summary and Conclusion

In this paper, we introduced EaR^{3}T, a toolbox that provides high-level interfaces to automate and facilitate 1D- and 3D-RT calculations. We presented applications that used EaR^{3}T to:

a) build a processing pipeline that can automatically simulate 3D radiance fields for satellite instruments (currently OCO-2 and MODIS) from publicly available satellite surface and cloud products at any given time over any specific region;
b) build a processing pipeline that can automatically simulate irradiance along all flight legs of aircraft missions, based on geostationary cloud products;
c) simulate radiance and irradiance for high-resolution COT fields retrieved from an airborne camera, using both a traditional 1D-RT (IPA) approach, and a newly developed 3D-RT (CNN) approach that considers the spatial context of a pixel.

Unlike other satellite simulators that employ 1D-RT, EaR^{3}T is capable of performing the radiance and irradiance calculations in 3D-RT mode. Optionally, it can be turned off to link back to traditional 1D-RT codes, and to calculate 3D perturbations by considering the changes of 3D-RT fields relative to the 1D-RT baseline.

With the processing pipeline under a) (App. 1 and App. 2, section 4), we prototyped a 3D-RT powered radiance loop that is envisioned for upcoming satellite missions such as EarthCARE and AOS. Retrieved cloud fields (in our case, from MODIS and from an airborne camera) are fed back into a 3D-RT simulation engine to calculate at-sensor radiances, which are then compared with the original measurements. Beyond currently included sensors, others can be added easily, taking advantage of the modular design of EaR^{3}T. This radiance closure loop facilitates the evaluation of passive imagery products, especially under spatially inhomogeneous cloud conditions. The automation of EaR^{3}T permits calculations at any time and over any given region, and statistics can be built by looping over entire orbits as necessary. The concept of radiance consistency could be valuable even for existing imagery datasets because it allows the automated quantification of 3D-RT biases even without ground truth such as airborne irradiance from suborbital activities. In the future it should be possible to include a 3D-RT pipeline such as EaR^{3}T into operational processing of satellite derived data products.

Benefitting from the automation of EaR^{3}T in b) (App. 3, section 5), we performed 3D-RT irradiance calculations for the entire CAMP^{2}Ex field campaign, moving well beyond radiation

Deleted: APP
Deleted: APP
Deleted: -
Deleted: APP

closure case studies, and instead systematically evaluating satellite-derived radiation fields with aircraft data for an entire region. From the comparison based on all below-cloud flight tracks during the entire campaign, we found that the satellite-derived cloud transmittance was biased low by 10% compared to the observations when relying on the heritage satellite cloud product.

From the statistical results of the CAMP[2]Ex irradiance closure in b), we concluded that the bias between satellite-derived irradiances and the ground truth from aircraft measurements was due to a combination of the coarse spatial resolution of the geostationary imagery products and 3D-RT effects. To minimize the coarse-resolution part of the bias and thus to isolate the 3D-RT bias, we used high-resolution airborne camera imagery in c) (App. 4, section 6), and found that even with increased imager resolution, biases persisted. The at-sensor radiance derived from IPA COT retrievals was inconsistent with the original measurements. For cloudy pixels, the calculated radiance was well below the observations, confirming an overall low bias in IPA COT. This low bias could be largely mitigated with the context-aware CNN developed separately in Nataraja et al. (2022) and included in EaR[3]T. Of course, this novel technique has limitations. For example, the camera reflectance data went beyond the CNN training envelope, which would need to be extended to larger COT in the future. In addition, the CNN only reproduces two-dimensional clouds fields and does not provide access to the vertical dimension, which will be the next frontier to tackle. Still, the greatly improved radiance consistency from COT_{IPA} to COT_{CNN} indicates that the EaR[3]T-LES-CNN approach shows great promise for the mitigation of 3D-RT biases associated with heritage cloud retrievals. We also discovered that for this particular case, the CRE calculated from traditional 1D cloud products can introduce a warm bias of at least 25% at the surface and above clouds.

EaR[3]T has proven to be capable of facilitating 3D-RT calculations for both remote sensing and radiative energy studies. Beyond the applications described in this paper, EaR[3]T has already been extensively used by a series of on-going research projects such as producing massive 3D-RT calculations as training data for a new generation of CNN models (Nataraja et al., 2022), evaluating 3D cloud radiative effects associated with aerosols (Gristey et al., 2022), creating flight track and satellite track simulations for mission planning etc. More importantly, the strategies provided in this paper put novel machine learning algorithms on a physical footing, opening the door for the mitigation of complexity-induced biases in the near-future. More development effort will be invested into EaR[3]T in the future, with the goals of minimizing the barriers to using 3D-RT

Deleted: either

Deleted: , or caused by

Deleted:

Deleted: APP

Deleted: warming

calculations, and to promote 3D cloud studies. EaR^{3}T will continue to be an educational tool driven by graduate students. In the future, we plan to add support for additional publicly available 3D RT solvers, e.g., SHDOM, as well as built-in support for HITRAN and associated correlated-k methods. From a research perspective, we anticipate that EaR^{3}T will enable the systematic quantification and mitigation of 3D-RT biases of imagery-derived cloud-aerosol radiative effects, and may be the starting point for operational use of 3D-RT for future satellite missions.

Deleted: it

Deleted: .

Appendix A - Technical Input Parameters of EaR^{3}T

EaR^{3}T provides various functions that can be combined to tailored pipelines for automatic 3D radiative transfer (3D-RT) calculations as described App. 1 – 5 of this paper (App. 1 – 5), as well as for complex research projects beyond. Since EaR^{3}T is written in Python, the modules and functions can be integrated into existing functions developed by the users themselves. Parallelization is enabled in EaR^{3}T by default through multi-processing to accelerate computations. If multiple CPUs are available, EaR^{3}T will distribute jobs for the 3D RT calculations. By default, the maximum number of CPUs will be used. Since EaR^{3}T is designed to make the process of setting up and running 3D-RT calculations simple, some parameters that are unavailable from the input data but are required by the RT solvers are populated via default values and assumptions. However, this does not mean that by using EaR^{3}T, one must use these assumptions; they can be easily superseded by user-provided settings. To facilitate this process, Table A1 provides a detailed list of parameters (subject to change in future updates) that can be controlled and modified by the user. In `examples/02_modis_rad-sim.py`, we defined these user-controllable parameters as global variables for providing easy access to user. In the future, most of the parameters will be controllable through a dedicated configuration file for optimal transparency. These parameters can be changed within the code. For instance, by changing the parameters of `_date` (Line 67 in `examples/02_modis_rad-sim.py`) and `_region` (Line 68 in `examples/02_modis_rad-sim.py`) into the following:

```
_date   = datetime.datetime(2022, 2, 10)
_region = [-6.8, -2.8, 17.0, 21.0]
```

one can perform similar RT calculations (as demonstrated in App. 2) for another date and region of interest (here, west Sahara Desert on 10 February, 2022). Note that the cloud detection algorithms we included in the code are imperfect (they only work satisfactorily for the App. 2 case we presented in this paper); for other regions on the globe, they may need to be adjusted. Automation of this feature is planned for the future. In addition, intuitive and simple examples are provided in `examples/00_er3t_mca.py` and `examples/00_er3t_lrt.py` for users who are interested in learning the basics of setting up EaR^{3}T for calculations. At the current stage, only limited documentation is provided. However, community support is available from the author of this paper through Discord[6]. In the near-future, more effort will be invested into documentation

[6] https://discord.gg/ntqsguwaWv

to give the user more autonomy in creating new applications that cannot be derived from those provided in our paper.

Parameters	App. 1 examples/01_oco2_rad-sim.py	App. 2 examples/02_modis_rad-sim.py	App. 3 examples/03_spns_flux-sim.py	App. 4 examples/04_cam_nadir_rad-sim.py	App. 5 examples/05_cnn-les_rad-sim.py
Date	September 2, 2019 Specified at Line 667: **date** And Line 626: **date**	September 2, 2019 Specified at Line 67: **_date** And Line 500: **date**	September 20, 2019 Specified at Line 442: **date** And Line 241: **date**	October 5, 2019 Specified at Line 390: **date** And Line 233: **date**	August 29, 2016 Specified at Line 222: **date**
Geographical Region	Specified at Line 668: **extent**	Specified at Line 68: **_region**	Variable (depends on aircraft location)	N/A	N/A
Z Grid (Number of Grids/Resolution)	40 / 0.5 km Specified at Line 547: **levels**	40 / 0.5 km Specified at Line 422: **levels**	20 / 1 km Specified at Line 184: **levels**	40 / 0.5 km Specified at Line 192: **levels**	20 / 1km Specified at Line 197: **levels**
Wavelength	770 nm Specified at Line 785: **wavelength**	650 nm Specified at Line 70: **_wavelength**	745 nm Specified at Line 443: **wavelength**	600 nm Specified at Line 57: **_wavelength**	600 nm Specified at Line 62: **wvl0**
Atmospheric Gas Profile	US standard atmosphere Specified at Line 549: **atm0**	US standard atmosphere Specified at Line 424: **atm0**	US standard atmosphere Specified at Line 186: **atm0**	US standard atmosphere Specified at Line 194: **atm0**	US standard atmosphere Specified at Line 200: **atm0**
Atmospheric Gas Absorption	Case specific Specified at Line 557: **abs0**	Default Absorption Database (Coddington et al., 2008) Specified at Line 431: **abs0**	Default Absorption Database (Coddington et al., 2008) Specified at Line 192: **abs0**	Default Absorption Database (Coddington et al., 2008) Specified at Line 201: **abs0**	Default Absorption Database (Coddington et al., 2008) Specified at Line 202: **abs0**
Cloud Top Height	From MODIS L2 cloud product Specified at Line 306: **cth_2d_l2** And Line 592: **cld0**	From MODIS L2 cloud product Specified at Line 280: **cth_2d_l2** And Line 466: **cld0**	From AHI L2 cloud product Specified at Line 211: **cth_2d** And Lines 215: **cld0**	2 km Specified at Line 217: **cth** And Lines 217: **cld0**	From LES Specified at Line 205: **cld0**
Cloud Geometrical Thickness	1 km Specified at Line 592: **cgt**	1 km And Line 466: **cgt**	1 km Specified at Line 215: **cgt**	1 km Specified at Line 217: **cgt**	From LES Specified at Line 205: **cld0**
Cloud Optical Thickness	Two-Stream Approximation for MODIS L1B Reflectance at 250 m resolution Specified at Line 402: **cot_2d_l1b** And Line 592: **cld0**	Two-Stream Approximation for MODIS L1B Reflectance at 250 m resolution Specified at Line 337: **cot_2d_l1b** And Line 466: **cld0**	From AHI L2 cloud product Specified at Line 201: **cot_2d** And Lines 215: **cld0**	Two-Stream Approximation and CNN for camera red channel radiance/reflectance at 100 m resolution Specified at Lines 285 and 324: **cot_ipa** and **cot_wei** And Lines 217: **cld0**	From LES Specified at Line 205: **cld0**
Cloud Effective Radius	From MODIS L2 Cloud Product Specified at Line 313: **cer_2d_l2**	From MODIS L2 Cloud Product Specified at Line 287: **cer_2d_l2**	From AHI L2 cloud product Specified at Line 202: **cer_2d**	12 micron Specified at Lines 285 and 380:	From LES Specified at Line 205: **cld0**

	And Line 592: `cld0`	And Line 466: `cld0`	And Lines 215: `cld0`	`cer_ipa` and `cer_2d` And Lines 217: `cld0`	
Scattering Phase Function	Mie Specified at Line 598: `pha0` And Line 630: `sca`	Mie Specified at Line 472: `pha0` And Line 504: `sca`	Mie Specified at Line 222: `pha0` And Line 240: `sca`	Henyey-Greenstein (g=0.85) Implicitly specified by default at Line 232: `mcarats_ng` Notes: Lines 207, 208, and 237 can be uncommented (meanwhile commenting out Line 209) to turn on Mie	Henyey-Greenstein (g=0.85) Implicitly specified by default at Line 221: `mcarats_ng`
Surface Albedo	From MODIS Surface Reflectance product and scaled by OCO-2 Specified at Line 520: `oco_sfc_alb_2d` And Line 629: `sfc_2d`	From MODIS Surface Reflectance product Specified at Line 395: `mod_sfc_alb_2d` And Line 503: `sfc_2d`	0.03 Implicitly specified by default at Line 237: `mcarats_ng`	0.03 Specified at Line 236: `surface_albedo`	0 Specified at Line 227: `surface_albedo`
Solar Zenith Angle	From OCO-2 geolocation file Specified at Line 615: `sza` And Line 633: `solar_zenith_angle`	From MODIS geolocation file Specified at Line 489: `sza` And Line 507: `solar_zenith_angle`	Variable (depends on aircraft location and date and time)	28.90° Specified at Line 352: `geometry['sza']` And Line 240: `solar_zenith_angle`	29.16° Specified at Line 228: `solar_zenith_angle`
Solar Azimuth Angle	From OCO-2 geolocation file Specified at Line 616: `saa` And Line 634: `solar_azimuth_angle`	From MODIS geolocation file Specified at Line 490: `saa` And Line 508: `solar_azimuth_angle`	Variable (depends on aircraft location and date and time)	296.83° Specified at Line 353: `geometry['saa']` And Line 241: `solar_azimuth_angle`	296.83° Specified at Line 229: `solar_azimuth_angle`
Sensor Altitude	705 km (satellite altitude) Implicitly specified by default at Line 625: `mcarats_ng`	705 km (satellite altitude) Implicitly specified by default at Line 499: `mcarats_ng`	N/A, three-dimensional irradiance outputs at user-defined Z grid	5.48 km (flight altitude) Specified at Line 354: `geometry['alt']` And Line 242: `sensor_altitude`	705 km (satellite altitude) Implicitly specified by default at Line 221: `mcarats_ng`
Sensor Zenith Angle	From OCO-2 geolocation file Specified at Line 617: `vza` And Line 635: `sensor_zenith_angle`	From MODIS geolocation file Specified at Line 491: `vza` And Line 509: `sensor_zenith_angle`	0° (nadir) Implicitly specified by default at Line 237: `mcarats_ng`	0° (nadir) Implicitly specified by default at Line 232: `mcarats_ng`	0° (nadir) Specified at Line 230: `sensor_zenith_angle`
Sensor Azimuth Angle	From OCO-2 geolocation file Specified at Line 618: `vaa`	From MODIS geolocation file Specified at Line 492: `vaa`	0° (insignificant for nadir)	0° (insignificant for nadir)	0° (insignificant for nadir) Specified at Line 231:

	And Line 636: `sensor_azimuth_angle`	And Line 510: `sensor_azimuth_angle`	Implicitly specified by default at Line 237: `mcarats_ng`	Implicitly specified by default at Line 232: `mcarats_ng`	`sensor_azimuth_angle`
Number of Photons	1×10^8 per run Specified at Line 72: `photon_sim` And Line 640: `photons`	1×10^8 per run Specified at Line 71: `photon_sim` And Line 514: `photons`	1×10^7 per run Specified at Line 56: `photon_sim` And Line 246: `photons`	1×10^8 per run Specified at Line 56: `photon_sim` And Line 246: `photons`	1×10^8 per run Specified at Line 66: `photon_sim` And Line 234: `photons`
Number of Runs	3 Specified at Line 638: `Nrun`	3 Specified at Line 512: `Nrun`	3 Specified at Line 245: `Nrun`	3 Specified at Line 244: `Nrun`	3 Specified at Line 233: `Nrun`
Mode (3D or IPA)	3D and IPA Specified at Line 786: `solver` And Line 641: `solver`	3D Specified at Line 620: `solver` And Line 515: `solver`	3D and IPA Specified at Lines 380 and 381: `solver` And Line 247: `solver`	3D Specified at Lines 391 and 392: `solver` And Line 247: `solver`	3D Specified at Line 210: `solver` And Line 236: `solver`
Parallelization Mode	Python multi-processing Specified at Line 643: `mp_mode`	Python multi-processing Specified at Line 517: `mp_mode`	Python multi-processing Specified at Line 250: `mp_mode`	Python multi-processing Specified at Line 249: `mp_mode`	Python multi-processing Specified at Line 238: `mp_mode`
Number of CPUs	8 Specified at Line 642: `Ncpu`	8 Specified at Line 516: `Ncpu`	16 Specified at Line 314: `Ncpu` And Line 249: `Ncpu`	12 Specified at Line 248: `Ncpu`	24 on clusters Specified at Line 237: `Ncpu`

Table A1: List of parameters used in the five applications. The line numbers used in the table are referring to the code script of each application. If two line numbers are provided, the first one indicates where the parameter is defined and the second one indicates where the parameter is passed into the radiative transfer setup. Users can change either one for customization purposes.

Appendix B – App. 5 Radiance calculations based on the Large Eddy Simulation

The CNN COT retrieval framework was developed by Nataraja et al. (2022). It adapts a U-Net (Ronneberger et al., 2015) architecture and treats the retrieval of COT from radiance as a segmentation problem – probabilities of 36 COT classes (ranging from COT of 0 to 100) are returned as the final COT retrieved for a given cloud radiance field. It accounts for horizontal photon transport, which is neglected in traditional cloud retrieval algorithms; in other words, for the spatial context of cloudy pixels. It was trained on synthetic cloud fields generated by a Large Eddy Simulation (LES) model, which provides the ground truth of COT. Subequently, EaR^{3}T was used to calculate 3D-RT radiances at 600 nm for LES cloud fields to establish a mapping between radiance to COT. Only six LES cases were used to represent the variability of the cloud morphology. Each of these fields are 480x480 pixels across (spatial resolution of 100 m). These large fields were mapped onto thousands of 64x64 mini tiles with spatial resolution of 100 m as described in Nataraja et al., 2022. To keep the training data set small, mini tiles selectively sampled according to their mean COT and standard deviation. This ensured an even representation of the dynamic range of COT and its variability, which was termed homogenization of the training data set. Figure A1 shows a collection of samples from the training data as an illustration. All the aforementioned simulation setup and techniques in data process are included in the App. 5 example code, which can be applied to the LES data (a different scene from the 6 scenes) distributed along with EaR^{3}T.

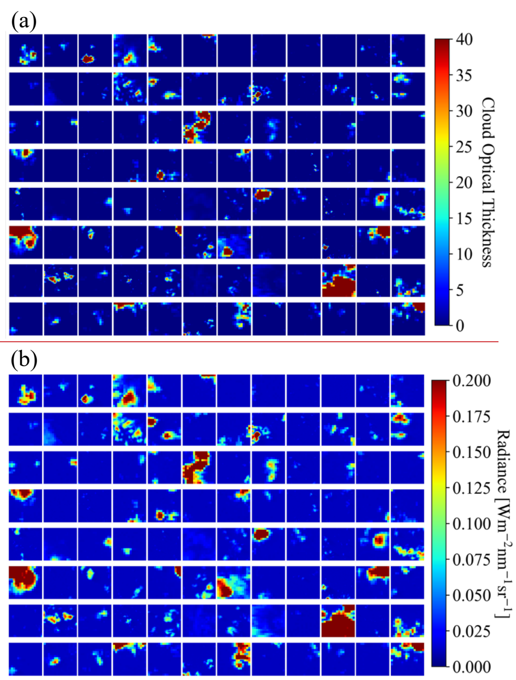

Figure A1. Illustrations of 64x64 tiles of **(a)** cloud optical thickness from LES data and **(b)** calculated 3D radiance from EaR^{3}T for CNN training.

Formatted: Font: Bold

Formatted: Font: Bold

Appendix C

Deleted: A

C1. Cloud Detection/Identification

Deleted: A1

Cloudy pixels are identified through a simple thresholding method based on the red, green, and blue channels of MODIS. When the radiance values of the red, green, and blue channels of a pixel are all greater than the corresponding median value, the pixel is considered as cloudy, as illustrated by the following equation

$$\textbf{If} \quad \begin{matrix} Red > Median(Red)\ \& \\ Blue > Median(Blue)\ \& \\ Green > Median(Green) \end{matrix} \begin{cases} \textbf{Yes}, \text{cloudy} \\ \textbf{No}, \text{clear sky} \end{cases} \qquad \text{(A1)}$$

Note that this only works for partially cloud-covered scenes, and may lead to false positives if there is brightness contrast from objects other than clouds. This method was specifically applied for the cases in this paper and should be changed as appropriate for future applications.

C2. Two-Stream Approximation

Deleted: A2

The two-stream approximation of the reflectance R is calculated using Eq. D2 from Chen et al. (2021), as follows:

$$R = \frac{\tau + \alpha \cdot \left(\frac{2\mu}{(1-g)\cdot(1-\alpha)}\right)}{\tau + \left(\frac{2\mu}{(1-g)\cdot(1-\alpha)}\right)} \qquad \text{(A2)}$$

where τ is the cloud optical thickness, α is the surface albedo, μ is the cosine of the solar zenith angle, and g is the asymmetry parameter. A value of 0.85 is assumed for g. The domain average of the solar zenith angle and surface albedo are calculated and used for estimating μ and α. Then, for a range of τ, we calculated the R and obtained the relationship of $R(\tau)$. For those cloudy pixels identified through A1, the inverse relationship of $\tau(R)$ is then used for estimating τ at any given R. Note that this approach does not take into account any cloud reflectance anisotropies.

Appendix D

Deleted: B

D1. Parallax Correction

Deleted: B1

From the satellite's view, the clouds (especially high clouds) will be placed at inaccurate locations on the surface, which have shifted from their actual locations due to the parallax effect. We followed simply trigonometry to correct for it, as follows:

Longitude correction (positive from west to east):

$$\delta lon = \frac{(z_{cld} - z_{sfc}) \cdot \tan(\theta) \cdot \sin(\phi)}{\pi \cdot R_{Earth}} \times 180° \quad \text{(B1)}$$

Latitude correction (positive from south to north):

$$\delta lat = \frac{(z_{cld} - z_{sfc}) \cdot \tan(\theta) \cdot \cos(\phi)}{\pi \cdot R_{Earth}} \times 180° \quad \text{(B2)}$$

where $(lon_{sat}, lat_{sat}, z_{sat})$ is the satellite location and θ and ϕ (0º at north, positive clockwise) are the sensor viewing zenith and azimuth angles. z_{cld} and z_{sfc} are the cloud top height and the surface height. R_{Earth} is the radius of the Earth. Figure A2 shows an illustration of parallax correction for the cloud field in the inset in Figure 2.

Deleted: A1

Deleted: black-boxed cloud field

D2. Wind Correction

Deleted: B2

The wind correction aims at correcting the movement of clouds when advected by the wind between two different satellites' overpasses.

Longitude correction (positive from west to east):

$$\delta lon = \frac{u \cdot \delta t}{\pi \cdot R_{Earth}} \times 180° \quad \text{(B3)}$$

Latitude correction (positive from south to north):

$$\delta lat = \frac{v \cdot \delta t}{\pi \cdot R_{Earth}} \times 180° \quad \text{(B4)}$$

where u and v are the domain-averaged 10 m zonal and meridional wind speeds, and δt is the time difference between two different satellites that fly on the same orbit. Figure A2 shows the cloud location after applying the parallax (Appendix D1) and wind correction for the cloud field in the inset from Figure 2.

Deleted: A1

Deleted: B1

Deleted: black box

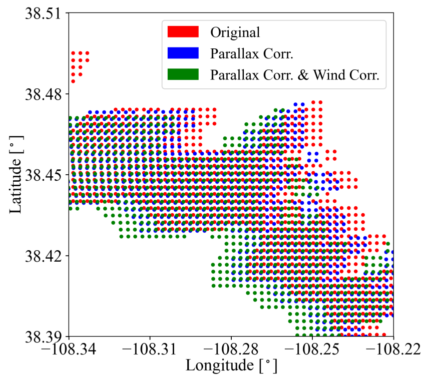

Figure A2. An illustration of correcting cloud location (red) for parallax effect (blue) and wind effect (green) for the cloud field of the inset in Figure 2.

Deleted: A1

Deleted: black-boxed

Acknowledgement

The aircraft all-sky camera was radiometrically calibrated by the U.S. Naval Research Laboratory. We thank Jens Redemann for insightful discussions about Figure 9 (App. 3) about the apparent contradiction of the direction of the COT, reflectance, and transmittance biases.

Data availability

For App. 1 and App. 2, the OCO-2 data were provided by the NASA Goddard Earth Sciences Data and Information Services Center (GES DISC, https://oco2.gesdisc.eosdis.nasa.gov/data) and the MODIS data were provided by the NASA Goddard Space Flight Center's Level-1 and Atmosphere Archive and Distribution System (LAADS, https://ladsweb.modaps.eosdis.nasa.gov/archive), which are all publicly available and can be downloaded by EaR^{3}T through the application code. For App. 3, the AHI data were processed by Holz's (coauthor of this paper) team. The SPN-S data were provided by Schmidt and Norgren (coauthors of this paper). Both the AHI and SPN-S data are publicly available at NASA Airborne Science Data for Atmospheric Composition (https://www-air.larc.nasa.gov/missions/camp2ex/index.html). The AHI data and the SPN-S data for the flight track indicated in Figure 8 of the paper are distributed along with EaR^{3}T for demonstration purpose. For App. 4, all sky camera imagery and CNN model are distributed along with EaR^{3}T. EaR^{3}T is publicly available and can be accessed and downloaded at https://github.com/hong-chen/er3t (or https://doi.org/10.5281/zenodo.7374196 for v0.1.0 used in this paper; Chen and Schmidt, 2022).

Author contributions

All the authors helped with editing the paper. HC developed the EaR^{3}T package in Python including the application code, performed the analysis, and wrote the majority of the paper with input from the other authors. SS provided MCARaTS simulation wrapper code in Interactive Data Language (IDL); helped with the structure design of EaR^{3}T; and helped with interpreting the results and writing the paper. SM helped with the OCO-2 data interpretation. VN trained and provided the CNN model. MN helped with the SPN-S instrument calibration and data processing. JG and GF helped with testing EaR^{3}T and the LES data interpretation. RH provided the AHI data and helped with the data interpretation. HI helped with the implementation of MCARaTS into EaR^{3}T.

References

Anderson, G. P., Clough, S. A., Kneizys, F. X., Chetwynd, J. H., and Shettle, E. P.: AFGL atmospheric constituent profiles (0–120 km), Tech. Rep. AFGL-TR-86–0110, Air Force Geophys. Lab., Hanscom Air Force Base, Bedford, Massachusetts, U.S.A., 1986.

Barker, H. and Liu, D.: Inferring optical depth of broken clouds from Landsat data, J. Climate, 8, 2620–2630, 1995.

Barker, H. W., Jerg, M. P., Wehr, T., Kato, S., Donovan, D. P., and Hogan, R. J.: A 3D cloud construction algorithm for the EarthCARE satellite mission, Q. J. Roy. Meteor. Soc., 137, 1042– 1058, https://doi.org/10.1002/qj.824, 2011.

Barker, H. W., Kato, S., and Wehr, T.: Computation of solar radiative fluxes by 1-D and 3-D methods using cloudy atmospheres inferred from A-train satellite data, Surv. Geophys., 33, 657–676, 2012.

Cahalan, R., Oreopoulos, L., Marshak, A., Evans, F., Davis, A., Pincus, R., Yetzen, K. H., Mayer, B., Yetzer, K. H., Mayer, B., Davies, R., Ackerman, T. P., Barker, H. W., Clothiaux, E. E., Ellingson, R. G., Garay, M. J., Kassianov, E., Kinne, S., Macke, A., O'Hirok, W., Partain, P. T., Prigarin, S. M., Rublev, A. N., Stephens, G. L., Szczap, F., Takara, E. E., Varnai, T., Wen, G., and Zhuravleva, T.: The I3RC: Bringing Together the Most Advanced Radiative Transfer Tools for Cloudy Atmospheres, B. Am. Meteorol. Soc., 86, 1275–1293, 2005.

Chen, H. and Schmidt, S.: er3t-v0.1.0, https://doi.org/10.5281/zenodo.7374196, 2022.

Chen, H., Schmidt, S., and Holz, R. E.: Synchronized Flight Videos for NASA CAMP^{2}Ex, https://doi.org/10.5281/zenodo.7358509, 2022.

Crisp, D.: Measuring Atmospheric Carbon Dioxide from Space with the Orbiting Carbon Observatory-2 (OCO-2), P. Soc. Photo.-Opt. Ins., 9607, 960702, https://doi.org/10.1117/12.2187291, 2015.

Coddington, O., Schmidt, K. S., Pilewskie, P., Gore, W. J., Bergstrom, R., Roman, M., Redemann, J., Russell, P. B., Liu, J., and Schaaf, C. C.: Aircraft measurements of spectral surface albedo and its consistency with ground-based and space-borne observations, J. Geophys. Res., 113, D17209, doi:10.1029/2008JD010089, 2008.

Deneke, H., Barrientos-Velasco, C., Bley, S., Hünerbein, A., Lenk, S., Macke, A., Meirink, J. F., Schroedter-Homscheidt, M., Senf, F., Wang, P., Werner, F., and Witthuhn, J.: Increasing the spatial resolution of cloud property retrievals from Meteosat SEVIRI by use of its high-resolution visible channel: implementation and examples, Atmos. Meas. Tech., 14, 5107–5126, https://doi.org/10.5194/amt-14-5107-2021, 2021.

Deutschmann, T., Beirle, S., Friess, U., Grzegorski, M., Kern, C., Kritten, L., Platt, U., Prados-Roman, C., Pukite, J., Wagner, T., Werner, B., and Pfeilsticker, K.: The Monte Carlo atmospheric radiative transfer model McArtim: introduction and validation of Jacobians and 3-D features, J. Quant. Spectrosc. Ra., 112(6), 1119–1137, ISSN 0022-4073, doi:10.1016/j.jqsrt.2010.12.009, 2011.

Doicu, A., Efremenko, D., and Trautmann, T.: A multi-dimensional vector spherical harmonics discrete ordinate method for atmospheric radiative transfer, J. Quant. Spectrosc. Ra., 118, 121–131, https://doi.org/10.1016/j.jqsrt.2012.12.009, 2013.

Emde, C., Barlakas, V., Cornet, C., Evans, F., Korkin, S., Ota, Y., Labonnote, L. C., Lyapustin, A., Macke, A., Mayer, B., and Wendisch, M.: IPRT polarized radiative transfer model intercomparison project – Phase A, Journal of Quantitative Spectroscopy and Radiative Transfer, 164, 8–36, https://doi.org/10.1016/j.jqsrt.2015.05.007, 2015.

Emde, C., Buras-Schnell, R., Kylling, A., Mayer, B., Gasteiger, J., Hamann, U., Kylling, J., Richter, B., Pause, C., Dowling, T., and Bugliaro, L.: The libRadtran software package for radiative transfer calculations (version 2.0.1), Geosci. Model Dev., 9, 1647–1672, https://doi.org/10.5194/gmd-9-1647-2016, 2016.

Evans, K. F.: The spherical harmonics discrete ordinate method for three-dimensional atmospheric radiative transfer, J. Atmos. Sci., 55, 429–446, 1998.

Gatebe, C. K., Jethva, H., Gautam, R., Poudyal, R., and Várnai, T.: A new measurement approach for validating satellite-based above-cloud aerosol optical depth, Atmos. Meas. Tech., 14, 1405–1423, https://doi.org/10.5194/amt-14-1405-2021, 2021.

Gristey, J. J., Feingold, G., Glenn, I. B., Schmidt, K. S., and Chen, H.: Surface Solar Irradiance in Continental Shallow Cumulus Fields: Observations and Large-Eddy Simulation, J. Atmos. Sci., 77, 1065–1080, https://doi.org/10.1175/JAS-D-19-0261.1, 2020a.

Gristey, J. J., Feingold, G., Glenn, I. B., Schmidt, K. S., and Chen, H.: On the Relationship Between Shallow Cumulus Cloud Field Properties and Surface Solar Irradiance, Geophysical Research Letters, 47, e2020GL090152, https://doi.org/10.1029/2020GL090152, 2020b.

Gristey, J. J., Feingold, G., Glenn, I. B., Schmidt, K. S., and Chen, H.: Influence of Aerosol Embedded in Shallow Cumulus Cloud Fields on the Surface Solar

Irradiance, Journal of Geophysical Research: Atmospheres, 127, e2022JD036822, https://doi.org/10.1029/2022JD036822, 2022.

Heidinger, A. K., Foster, M. J., Walther, A., and Zhao, X.: The Pathfinder Atmospheres-Extended AVHRR climate dataset, B. Am. Meteorol. Soc., 95, 909–922, https://doi.org/10.1175/BAMS-D-12-00246.1, 2014.

Illingworth, A. J., Barker, H. W., Beljaars, A., Chepfer, H., Delanoe, J., Domenech, C., Donovan, D. P., Fukuda, S., Hirakata, M., Hogan, R. J., Huenerbein, A., Kollias, P., Kubota, T., Nakajima, T., Nakajima, T. Y., Nishizawa, T., Ohno, Y., Okamoto, H., Oki, R., Sato, K., Satoh, M., Wandinger, U., Wehr, T., and van Zadelhoff, G.: The EarthCARE Satellite: the next step forward in global measurements of clouds, aerosols, precipitation and radiation, B. Am. Meteorol. Soc, 96, 1311–1332, https://doi.org/10.1175/BAMS-D-12-00227.1, 2015.

Iwabuchi, H.: Efficient Monte Carlo methods for radiative transfer modeling, J. Atmos. Sci., 63, 2324–2339, 2006.

Kindel, B. C., Schmidt, K. S., Pilewskie, P., Baum, B. A., Yang, P., and Platnick, S.: Observations and modeling of ice cloud shortwave spectral albedo during the Tropical Composition, Cloud and Climate Coupling Experiment (TC^4), J. Geophys. Res., 115, D00J18, doi:10.1029/2009JD013127, 2010.

King, M., and Platnick, S.: The Earth Observing System (EOS), Comprehensive Remote Sensing, 7, 26, doi:10.1016/b978-0-12-409548-9.10312-4, 2018.

Levis, A., Schechner, Y. Y., Davis, A. B., and Loveridge, J.: Multi-View Polarimetric Scattering Cloud Tomography and Retrieval of Droplet Size, Remote Sens., 12, 2831, https://doi.org/10.3390/rs12172831, 2020.

Li, J., Scinocca, J., Lazare, M., McFarlane, N., von Salzen, K., and Solheim, L.: Ocean Surface Albedo and Its Impact on Radiation Balance in Climate Models, J. Climate, 19, 6314–6333, 2006.

Long, C. N., Bucholtz, A., Jonsson, H., Schmid, B., Vogelmann, A., and Wood, J.: A Method of Correcting for Tilt from Horizontal in Downwelling Shortwave Irradiance Measurements on Moving Platforms, The Open Atmospheric Science Journal, 4, 78–87, 2010.

Loveridge, J., Levis, A., Di Girolamo, L., Holodovsky, V., Forster, L., Davis, A. B., and Schechner, Y. Y.: Retrieving 3D distributions of atmospheric particles using Atmospheric Tomography with 3D Radiative Transfer – Part 1: Model description and Jacobian calculation, Atmos.

Meas. Tech. Discuss. [preprint], https://doi.org/10.5194/amt-2022-251, in review, 2022.

Masuda, R., Iwabuchi, H., Schmidt, K. S., Damiani, A. and Kudo, R.: Retrieval of Cloud Optical Thickness from Sky-View Camera Images using a Deep Convolutional Neural Network based on Three-Dimensional Radiative Transfer, Remote Sensing, 11(17), 1962, doi:10.3390/rs11171962, 2019.

Marshak, A., Davis, A., Wiscombe, W., and Cahalan, R.: Radiative smoothing in fractal clouds, J. Geophys. Res., 100, 26247–26261, https://doi.org/10.1029/95JD02895, 1995.

Marshak, A., Wen, G., Coakley, J., Remer, L., Loeb, N. G., and Cahalan, R. F.: A simple model for the cloud adjacency effect and the apparent bluing of aerosols near clouds, J. Geophys. Res., 113, D14S17, https://doi.org/10.1029/2007JD009196, 2008.

Massie, S. T., Schmidt, K. S., Eldering, A., and Crisp, D.: Observational evidence of 3-D cloud effects in OCO-2 CO2 retrievals, J. Geophys. Res. Atmos., 122, 7064–7085, https://doi.org/10.1002/2016JD026111, 2017.

Mayer, B. and Kylling, A.: Technical note: The libRadtran software package for radiative transfer calculations – description and examples of use, Atmos. Chem. Phys., 5, 1855–1877, https://doi.org/10.5194/acp-5-1855-2005, 2005.

Mayer, B.: Radiative transfer in the cloudy atmosphere, EPJ Web of Conferences, 1, 75–99, doi:10.1140/epjconf/e2009-00912-1, 2009.

Mlawer, E. J., Taubman, S. J., Brown, P. D., Iacono, M. J., and Clough, S. A.: Radiative transfer for inhomogeneous atmospheres: RRTM, a validated correlated-k model for the longwave, J. Geophys. Res., 102, 16663–16682, 1997.

Nakajima, T. and King, M. D.: Determination of the optical thickness and effective particle radius of clouds from reflected solar radiation measurements. Part I: Theory, J. Atmos. Sci., 47, 1878–1893, 1990.

Nataraja, V., Schmidt, S., Chen, H., Yamaguchi, T., Kazil, J., Feingold, G., Wolf, K., and Iwabuchi, H.: Segmentation-Based Multi-Pixel Cloud Optical Thickness Retrieval Using a Convolutional Neural Network, Atmos. Meas. Tech., 15, 5181–5205, doi:10.5194/amt-15-5181-2022, 2022.

Norgren, M. S., Wood, J., Schmidt, K. S., van Diedenhoven, B., Stamnes, S. A., Ziemba, L. D., Crosbie, E. C., Shook, M. A., Kittelman, A. S., LeBlanc, S. E., Broccardo, S., Freitag, S., and Reid, J. S.: Above-aircraft cirrus cloud and aerosol optical depth from hyperspectral

Deleted: Atmos. Meas. Tech. Discuss. [preprint], https://doi.org/10.5194/amt-2022-45, in review, 2022.

irradiances measured by a total-diffuse radiometer, Atmos. Meas. Tech., 15, 1373–1394, https://doi.org/10.5194/amt-15-1373-2022, 2022.

Payne, V. H., Drouin, B. J., Oyafuso, F., Kuai, L., Fisher, B. M., Sung, K., Nemchicka, D., Crawford, T. J., Smyth, M., Crisp, D., Adkins, E., Hodges, J. T., Long, D. A., Mlawer, E. J., Merrelli, A., Lunny, E., and O'Dell, C. W.: Absorption coefficient (ABSCO) tables for the Orbiting Carbon Observatories: version 5.1, J. Quant. Spectrosc. Ra., 255, 1–16, https://doi.org/10.1016/j.jqsrt.2020.107217, 2020.

Pilewskie, P., Pommier, J., Bergstrom, R., Gore, W., Howard, S., Rabbette, M., Schmid, B., Hobbs, P. V., and Tsay, S. C.: Solar spectral radiative forcing during the Southern African Regional Science Initiative, J. Geophys. Res., 108, 8486, https://doi.org/10.1029/2002JD002411, 2003.

Pincus, R. and Evans, K. F.: Computational cost and accuracy in calculating three-dimensional radiative transfer: Results for new implementations of Monte Carlo and SHDOM, J. Atmos. Sci., 66, 3131–3146, 2009.

Platnick, S., King, M. D., Ackerman, S. A., Menzel, W. P., Baum, B. A., Riédi, J. C., and Frey, R. A.: The MODIS cloud products: Algorithms and examples from Terra, IEEE T. Geosci. Remote, 41, 459–473, 2003.

Reid, J. S., Maring, H. B., Narisma, G., van den Heever, S., DiGirolamo, L., Ferrare, R., Lawson, P., Mace, G. G., Simpas, J., Tanelli, S., Ziemba, L., van Diedenhoven, B., Bruintjes, R., Bucholtz, A., Cairns, B., Cambaliza, M. O., Chen, G., Diskin, G. S., Flynn, J. H., Hostetler, C. A., Holz, R. E., Lang, T. J., Schmidt, K. S., Smith, G., Sorooshian, A., Thompson, E. J., Thornhill, K. L., Trepte, C., Wang, J., Woods, S., Yoon, S., Alexandrov, M., Alverez, S., Amiot, C., Bennett, J. R., Brooks, M., Burton, S. P., Cayanan, E., Chen, H., Collow, A., Crosbie, E., DaSilva, A., DiGangi, J. P., Flagg, D. D., Freeman, S. W., Fu, D., Fukada, E., Hilario, M. R. A., Hong, Y., Hristova-Veleva, S. M., Kuehn, R., Kowch, R. S., Leung, G. R., Loveridge, J., Meyer, K., Miller, R., Montes, M. J., Moum, J. N., Nenes, T., Nesbit, S. W., Norgen, M., Novak, E., Rauber, R. M., Reid, E. A., Rutledge, S., Schlosser, J. S., Sekiyama, T. T., Shook, M. A., Sokolowsky, G. A., Stamnes, S. A., Sy, O. O., Tanaka, T. Y., Wasilewski, A., Xian, P., Xiao, Q., and Zavaleta, J.: The coupling between tropical meteorology, aerosol lifecycle, convection, and radiation, during the Clouds, Aerosol and Monsoon Processes Philippines Experiment (CAMP^{2}Ex), B. Am. Meteorol. Soc., *in review*, 2022.

Ronneberger, O., Fischer, P., and Brox, T.: U-net: Convolutional networks for biomedical image segmentation, in: International Conference on Medical image computing and computer-assisted intervention, 234–241, Springer, https://doi.org/10.1007/978-3- 319-24574-4_28, 2015.

Rothman, L., Jacquemart, D., Barbe, A., Chris Benner, D., Birk, M., Brown, L., Carleer, M., Chackerian, C., Chance, K., Coudert, L., Dana, V., Devi, V., Flaud, J.-M., Gamache, R., Gold- man, A., Hartmann, J.-M., Jucks, K., Maki, A., Mandin, J.- Y., Massie, S., Orphal, J., Perrin, A., Rinsland, C., Smith, M., Tennyson, J., Tolchenov, R., Toth, R., Vander Auwera, J., Varanasi, P., and Wagner, G.: The HITRAN 2004 molecular spectroscopic database, J. Quant. Spectrosc. Ra., 96, 139–204, https://doi.org/10.1016/j.jqsrt.2004.10.008, 2005.

Schmidt, K. S., Pilewskie, P., Platnick, S., Wind, G., Yang, P., and Wendisch, M.: Comparing irradiance fields derived from Moderate Resolution Imaging Spectroradiometer airborne simulator cirrus cloud retrievals with solar spectral flux radiometer measurements, J. Geophys. Res., 112, D24206, doi:10.1029/2007JD008711, 2007.

Schmidt, S., Pilewskie, P., Mayer, B., Wendisch, M., Kindel, B., Platnick, S., King, M. D., Wind, G., Arnold, G. T., Tian, L., Heymsfield, G., and Kalesse, H.: Apparent absorption of solar spectral irradiance in heterogeneous ice clouds, J. Geophys. Res., 115, D00J22, https://doi.org/10.1029/2009JD013124, 2010.

Schmidt, S., Massie, S., Chen, H., Crisp, D., Kulawik, S., Chen, Y.-W., Merrelli, A., McDuffie, J., Iwabuchi, H.: Uncovering the Mechanism for Trace Gas Spectroscopy Biases in the Vicinity of Clouds With the OCO-2 3D Radiative Transfer Satellite Radiance Simulator, Atmos. Meas. Tech., *in prep.*, 2022.

Song, S., Schmidt, K. S., Pilewskie, P., King, M. D., Heidinger, A. K., Walther, A., Iwabuchi, H., Wind, G., and Coddington, O. M.: The Spectral Signature of Cloud Spatial Structure in Shortwave Irradiance, Atmos. Chem. Phys., 16, 13791–13806, https://doi.org/10.5194/acp-16-13791-2016, 2016.

Spada, F., Krol, M. C., and Stammes, P.: McSCIA: application of the Equivalence Theorem in a Monte Carlo radiative transfer model for spherical shell atmospheres, Atmos. Chem. Phys., 6, 4823–4842, https://doi.org/10.5194/acp-6-4823-2006, 2006.

Vermote, E. F., Roger, J. C., and Ray J. P.: MODIS Surface Reflectance User's Guide, MODIS Land Surface Reflectance Science Computing Facility, Version 1.4, 1-35, 2015.

Wood, J., Smyth, T. J., and Estellés, V.: Autonomous marine hyperspectral radiometers for

Deleted: -

determining solar irradiances and aerosol optical properties, Atmos. Meas. Tech., 10, 1723–1737, https://doi.org/10.5194/amt-10-1723-2017, 2017.

Page 22: [1] Deleted Hong Chen 12/6/22 5:16:00 PM